September 1, 1996

Observationsof inner-plasmasphere irregularities with a satellite beacon interferometer array

A. R. Jacobsen
G. Hogeveen
R. C. Carlos
G. Wu
Bela G. Fejer, *Utah State University*, et al.

JOURNAL OF GEOPHYSICAL RESEARCH, VOL. 101, NO. A9, PAGES 19,665–19,682, SEPTEMBER 1, 1996

Observations of inner plasmasphere irregularities with a satellite-beacon radio-interferometer array

Abram R. Jacobson, Gary Hoogeveen, Robert C. Carlos, and Guanghui Wu

Space and Atmospheric Sciences Group, Los Alamos National Laboratory, Los Alamos, New Mexico

Bela G. Fejer

Center for Atmospheric and Space Sciences, Utah State University, Logan

Michael C. Kelley

School of Electrical Engineering, Cornell University, Ithaca, New York

Abstract. A radio-interferometer array illuminated by 136-MHz beacons of several geosynchronous satellites has been used to study small ($\geq 10^{13}$ m^{-2}) transient disturbances in the total electron content along the lines of sight to the satellites. High-frequency ($f > 3$ mHz) electron content oscillations are persistently observed, particularly during night and particularly during geomagnetically disturbed periods. The oscillations move across the array plane at speeds in the range 200-2000 m/s, with propagation azimuths that are strongly peaked in lobes toward the western half-plane. Detailed analysis of this azimuth behavior, involving comparison between observations on various satellite positions, indicates compellingly that the phase oscillations originate in radio refraction due to geomagnetically aligned plasma density perturbations in the inner plasmasphere. The motion of the phase perturbations across the array plane is caused by **EXB** drift of the plasma medium in which the irregularities are embedded. We review the statistics of 2.5 years of around-the-clock data on the local time, magnetic disturbance, seasonal, and line-of-sight variations of these observed irregularities. We compare the irregularities' inferred electrodynamic drifts to what is known about midlatitude plasma drift from incoherent scatter. Finally, we show in detail how the observation of these irregularities provides a unique and complementary monitor of inner plasmasphere irregularity incidence and zonal drift.

1. Background

The plasmasphere is known to contain plasma density irregularities on many scales. Most basic is its idealized outer boundary, the plasmapause, on which much of the original observations were made with whistler waves [*Carpenter*, 1966]. More recent satellite studies [*Horwitz et al.*, 1990] reveal that the plasmapause, far from being the only steep gradient in plasma density, is a simple case from among a varied set of gradient regimes, in which there may be more than one sharp density shelf. In addition, in situ measurements of electron density in the range $L \sim 3$-6 show that there are apparently irregular, local perturbations quite distinct from the shelves [*LeDocq et al.*, 1994]. Finally, the guided propagation of whistlers between conjugate hemispheres is forcedly due to ducts greatly elongated along the geomagnetic field, but their morphology remains obscure [*Angerami*, 1970]: Are the ducts' cross-sectional shapes sheetlike, extended within magnetic meridians, or flutelike, resembling round tubes? Is a duct solitary, or does it occur as part of a spatially oscillatory structure? Neither whistler data nor satellite in situ flythroughs have answered these questions.

Paper number 96JA01253.
0148-0227/96/96JA-01253$09.00

A new and complementary approach to observing at least inner plasmaspheric irregularities has shed some additional light on irregularity shape and disposition. Campaigns with the Very Large Array (VLA) radio telescope array, using astrometric "calibrator" unresolved extragalactic radiosources, revealed the presence of flute-like density perturbations in the inner plasmasphere, each flute having a cross section that was more round than sheet-like [*Jacobson and Erickson*, 1993]. Most surprisingly, the perturbations seen with the VLA occurred in coherent bursts of alternating flutes of overdensities and underdensities, with the flutes separated in magnetic longitude. That is, a spatial perturbation was localized in L (the McIlwain parameter identifying magnetic shells), extended along **B**, and cyclical in the magnetic zonal direction (i.e., within the magnetic shell). The magnetic zonal angular separation between successive density enhancements was typically in the range of a few milliradians; the relative density perturbations were of the order $\delta n/n \sim 0.1$, and the L shells in which the perturbations were observed in the range $L \sim 2$ - 3. All of these ranges may have been at least partially constrained by sensitivity and geometrical constraints of the observing scheme itself [*Jacobson and Erickson*, 1993 and G. W. Hoogeveen and A. R. Jacobson, Improved analysis of plasmaspheric motion using the very large array radio-interferometer, submitted to *Annal. Geophysics*, 1995, hereinafter referred to as submitted manuscript, 1995] and are not necessarily inherent in the irregularities per se. What is

indisputable about these VLA observations, though, is that the observed inner plasmasphere density perturbations occur in zonally oscillating bursts localized to magnetic shells and greatly extended along **B**. This was the first diagnostic capable of detecting and resolving the fine-scale zonal morphology of inner plasmasphere irregularities, and in this sense complemented in situ and whistler information.

Recently, an extremely sensitive very long baseline interferometer (VLBI) array, illuminated by geosynchronous satellite beacons, has been deployed for around-the-clock observations of geoplasma irregularities [*Carlos and Massey*, 1994]. It constitutes a more sensitive, cost-effective, and available facility than does the VLA for this application and has already been used for studies of traveling ionospheric disturbance (TID) climatology [*Jacobson et al.*, 1995a].

It has also been briefly reported [*Jacobson et al.*, 1995b] that the new VLBI array detects plasmaspheric irregularities but with a crucial difference from the manner in which the VLA did this: In the case of either instrument, the observation of plasmaspheric irregularities is possible only to the extent that their interferometric phase signatures are sufficiently elevated in frequency to be above the continuum of the far more intense TEC (total electron content) perturbations due to TIDs. In practice, this means that the phase oscillations due to plasmaspheric irregularities must have frequencies $f > (1\text{-}3)$ mHz, the exact limit depending on season and local time [*Jacobson et al.*, 1995a]. Now, since the irregularities seem to be quasi-frozen in the plasmasphere, at any rate evolving in the plasma frame-of-reference at rates which are weak compared to this requisite observed frequency, it follows that the observed frequency must be supplied "artificially." With the VLA, this artificial frequency was created by the westward slip, with respect to the approximately geocorotating inner plasmasphere, of the radio lines-of-sight tracking the celestial radio sources. With the geosynchronous satellite beacon array, on the other hand, there is sensibly no slip between the lines of sight and the geocorotating frame, and thus the only way to introduce a nonzero frequency is for the plasma medium to drift (at the velocity $\mathbf{E}\times\mathbf{B}/B^2$) with respect to the geocorotating frame. Thus, unlike the VLA observations, the satellite-beacon observations described below depend in an essential manner not only on the irregularities' existence but also on the contemporary convection of the plasma medium in which the irregularities are embedded. While somewhat complicating the irregularities' observability, this second condition also offers the potential to monitor inner plasmasphere convection by an entirely novel passive-tracer approach.

2. Apparatus and Method

The present array (Figure 1) contains nine autonomous receiver stations centered on Los Alamos, New Mexico (35.87° N, 106.33° W). The hardware, the data compression algorithm, and each site computer's multitasking scheme have been described in detail elsewhere [*Carlos and Massey*, 1994]. The performance of the array has been described in detail with respect to TID climatology [*Jacobson et al.*, 1995a], so here we merely reiterate that the array continuously measures the difference of slant TEC between ends of any baseline formed by a pair of stations within the array. This difference, called "baseline-differenced TEC," is measured with an instrumental ms noise level of $(1\text{-}5)\times10^{12}$ m^{-2} in the spectral band 3-30 mHz. Since this is of the order of 10^{-5} of a typical slant background TEC, the array is sensitive to exceedingly subtle electron density perturbations, including those residing in the relatively low background density (10^9 - 10^{10} m^{-3}) inner plasmasphere. In Figure 1, the core triangle (stations l, a, g, and y) are nearly the original array [*Jacobson et al.*, 1995a], while both the two short-baseline stations (k, h) and the three very long-baseline stations (c, v, and z) are new and were hence available for only a subset of the data included in this study.

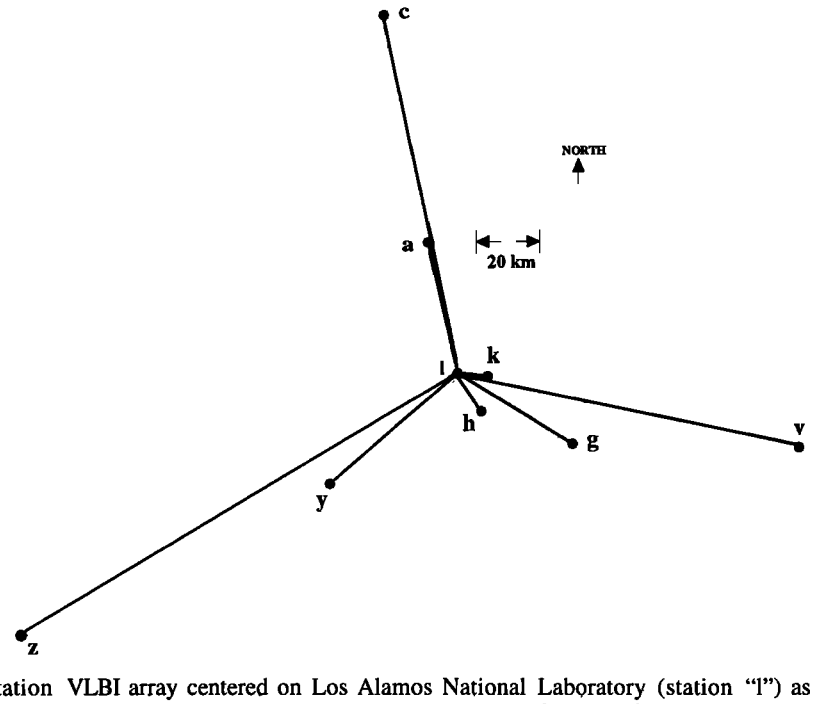

Figure 1. The nine-station VLBI array centered on Los Alamos National Laboratory (station "l") as of spring 1995. The subset containing stations "l," "a," "g," and "y" were the earlier array (*Jacobson et al.* 1995a].

The interferometer is illuminated by the VHF ~136-MHz beacons carried by several geosynchronous satellites. The conversion between TEC and electrical carrier phase is ~1.6×10^{14} m^{-2} rad^{-1}. Those satellites which we have used during at least parts of this study are GOES 2, GOES 3, ATS-1, and ATS-3. Except for ATS-3, which stayed at a constant longitude nearly in the Los Alamos meridian all through this experiment, the other satellites have drifted (in the case of ATS-1) and been moved (in the cases of GOES 2 and GOES 3) over longitude. Therefore we use detailed and regularly updated orbital element sets to calculate each satellite's instantaneous position for the periods in which its beacon is used. Each array station has three separate receiver channels, so we have the ability to perform interferometry along three independent clusters of lines of sight (when three satellites are available.) Figure 2 (top) shows baseline phase versus time during a window containing 256 samples spaced by 8.74 s. The baselines are between each of seven outlier stations and the central station (l) at Los Alamos. The data were taken on May 3, 1995 starting at 0323 UT (local evening), so TIDs (characterized by periods of 1000-2000 s) do not figure prominently [*Jacobson et al.*, 1995a]. Instead, as is typical of night, the phase perturbations are weak but high-frequency. Figure 2 (bottom) also shows the Fourier spectra of the phase variations for the same 256-sample time-window. In the work described here we will confine attention to spectral peaks in the passband 3-9 mHz. The requirement of spectral peakedness selects for monochromatic signatures, in which the chance of multidisturbance overlap is usefully reduced [*Jacobson et al.*, 1995a]. The requirement will quantitatively be that the peak spectral density averaged over all baselines exceed, by at least a factor 1.5, the neighboring spectral density troughs on either side of the peak. The passband requirement (i.e., 3-9 mHz) is set (on the low end) by a need absolutely to avoid TID contamination, and (on the high end) by the lack, in practice, of sensible TEC perturbations shorter-period than ~100 s. The two spectral peaks in Figure 2 satisfying these criteria are at 4.47 and 5.81 mHz.

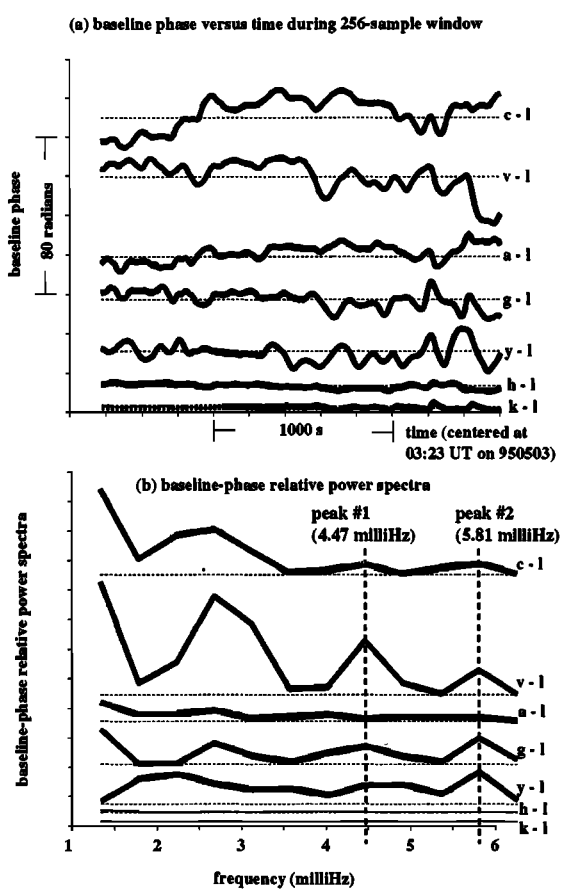

Figure 2. (a) Baseline phase versus time on each of seven baselines terminating in Los Alamos, for a 256-sample (2237-s) window centered on 0323 UT on May 3, 1995. (b) Relative power spectra for the above baseline-phase data in the band ~ 1.3 - 6.3 mHz. Two spectral peaks at $f > 3$ mHz are indicated. Each trace's corresponding baseline is indicated.

As in previous work with this array, we advance the Fourier window by only 1/8 (rather than 1/2) of its width, thereby somewhat overestimating the number of truly independent peak detections.

The next step in analyzing the data is applied to the complex Fourier coefficients $\Phi_{mn}(\omega)$ of the baseline phases on all baselines m,n. At each ω, we estimate the TEC-perturbation amplitude $A(\omega)$ and horizontal wave vector $\boldsymbol{k}(\omega)$ using the ensemble of $\Phi_{mn}(\omega)$ as data in a least squares fit to the model

$$\hat{N}(\omega) = A(\omega)\exp\{-i\boldsymbol{k}\cdot\boldsymbol{r}\} \qquad (1)$$

of the causative TEC perturbation $N(\omega)$. Here $\boldsymbol{r}$ is the horizontal position vector in the array plane. It is convenient to use slowness (the inverse of horizontal phase velocity, that is, $S(\omega)$ (= $k(\omega)/\omega$)) instead of velocity in characterizing the solution's $\boldsymbol{k}$. In cases where the selected peak contains more than one frequency, we constrain the slowness vector to be a constant. Thus the fitted parameters are S_x (eastward slowness) and S_y (northward slowness) for all frequencies in the peak, and a real and an imaginary component of A for each frequency in the peak. Various tradeoffs and complications of this method have been described in detail elsewhere [*Jacobson and Erickson*, 1992a, b, 1993; *Jacobson et al.*, 1995a]. It suffices here to reiterate that the products of analyzing a given peak are (1) a slowness vector and (2) as many complex-amplitude coefficients as there are Fourier frequencies in the spectral peak. In the work reported here, peaks are further selected by three requirements on these least square solutions: First, the rms TEC amplitude integrated over the peak must exceed 1×10^{12} m^{-2}. Second, the sum of the squares of the fit residuals must be less than 0.05 times the sum of the squares of the data; this is a "goodness of fit" measure. Third, the trace wavelength must exceed 75 km, so that we avoid spatial aliasing for that substantial portion of the campaign when stations k and h were lacking (*Jacobson et al.* 1995a). Referring to Figure 2, both of the labeled peaks survive this down-selection. The peak 1 TEC disturbance moves across the array at a fitted trace speed (i.e., $1/S$) 787 m/s, while the peak 2 TEC disturbance moves across the array at a fitted trace speed 811 m/s, and both are directed approximately toward an azimuth -80°. We will use the term "azimuth" to indicate the direction of the $\boldsymbol{k}$ or $\boldsymbol{S}$ vector on the interferometer plane, that is, the direction toward which the wave propagates. In the following, when a spectral peak is sufficiently peaked and lies in the selected spectral range, and when additionally its least-squares solution satisfies the amplitude and goodness-of-fit criteria just stated, than we will call that wavelike disturbance an "event."

3. Unusual Features of the Data

Like those seen with the VLA [*Jacobson and Erickson*, 1993], the high-frequency disturbances seen with the Los Alamos VLBI array have several unusual features that are difficult to explain by invoking ionospheric processes. Foremost of these features is the high frequency itself, well above the range of Brunt-Vaisala buoyancy frequencies in the thermosphere, and hence well above the allowed range of buoyancy wave frequencies. Second, the trace speeds are in the range 200 - 2000 m/s, at least the higher end of which is difficult to ascribe to thermospheric acoustic waves. Third, and certainly most telling against a hypothesis that these high-frequency TEC disturbances are due to waves at ionospheric heights, are the glaring dissimilarities between TEC disturbances seen with lines of sight to different satellites.

This dissimilarity can be seen in the relative appearance of contemporary baseline-phase data using more than one satellite. Figure 3 shows baseline-phase data on identical sets of baselines for ATS-3 (Figure 3a) and GOES 2 (Figure 3b) at a time when those two satellites were separated by ~30° in longitude, for a ~3-hour window beginning at 0250 UT on October 12, 1994. The appearances of the phase data are completely different between the lines of sight to the two satellites, even though any given station's lines of sight to the two satellite puncture the *F* layer only ~200 km from each other. By examining the propagation solutions (see above) of the disturbances seen with either satellite, it can be shown that the trace wavelengths are of the order of 100 - 300 km, so it would be absurd for there to be such a dissimilarity between disturbances from *F* layer regions separated horizontally by what is only a single disturbance wavelength. The only way out of this absurdity is to admit that the disturbances may reside higher up on the lines of sight, where their separation would be of the order of several thousand kilometers.

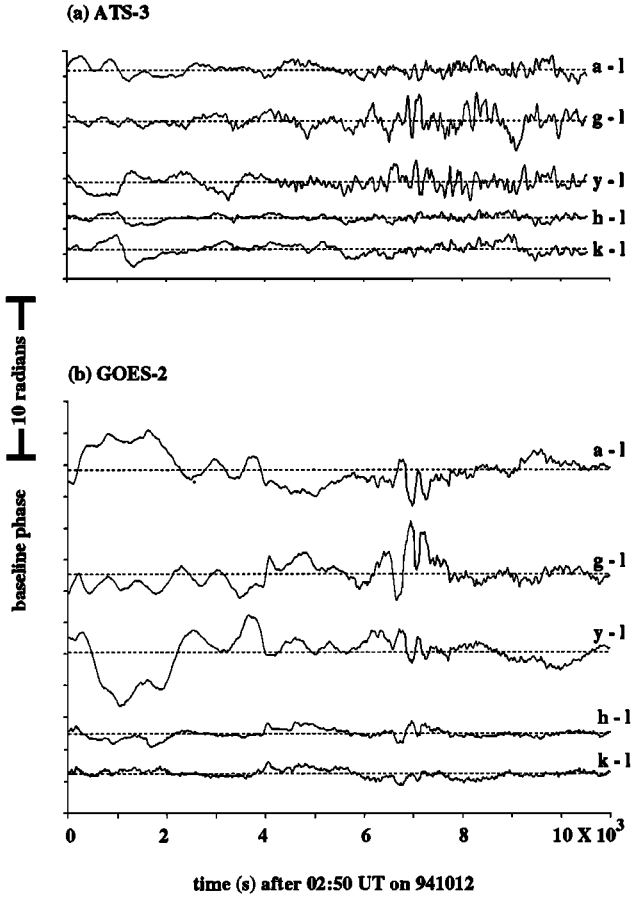

Figure 3. Contemporaneous baseline-phase time series for lines of sight to (a) ATS-3 (top) and to (b) GOES 2 (bottom) during ~11,000 s starting at 0250 UT on October 12, 1994. Each trace's corresponding baseline is indicated.

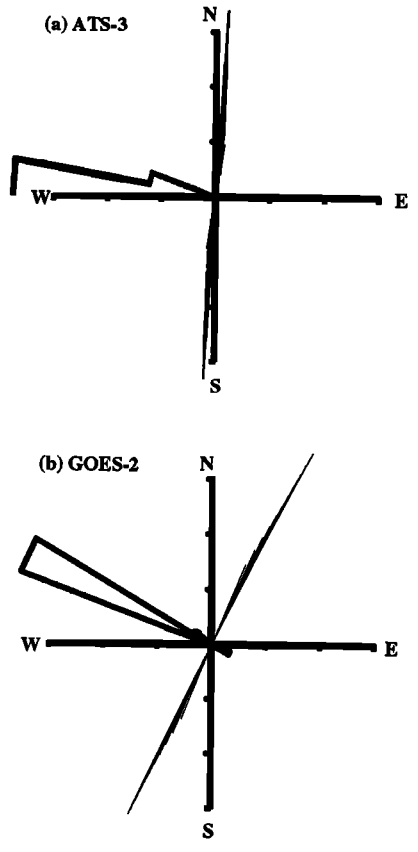

Figure 4. Polar plots of event-azimuth distributions for the data of Figure 3 above. The superimposed sheaths of straight lines will be explained in the text later. The radius is proportional to histogram counts.

We can submit the data in Figure 3 from each satellite during those ~3 hours to a peak finding analysis and then an event downselection (as described above, in reference to Figure 2). Doing this, we obtain 12 acceptable events for GOES 2 and 16 acceptable events for ATS-3 lines of sight. Figure 4 shows polar plots of the azimuth distribution of these events. (The narrow clusters of straight lines will be discussed later in this paper.) Two things are apparent: First, the azimuth distribution for each satellite's data is quite narrow. Second, the two distributions are significantly different from each other. Modeling of the efficiency of atmospheric waves at ionospheric heights in generating slant-TEC perturbations [*Georges and Hooke*, 1970; *Bertel et al.*, 1976] indicates that instrumental-bias azimuth lobes (due to viewing geometry, etc.) exist but are much wider (of the order of 150°) than either lobe seen here in Figure 4. Therefore the lobes in Figure 4 must owe their narrowness to some other effect. Moreover, lines of sight differing by tens of degrees (as in this case) may

detect an ionospheric disturbance of given azimuth with varying efficiency, but nonetheless interpret that azimuth without bias [*Mercier*, 1986] We conclude that contemporary observations of high-frequency TEC disturbances, with lines of sight to different satellites, do not support an ionospheric explanation of these data.

The next level at which to demonstrate the difficulty of an ionospheric model for these disturbances is to examine event-azimuth patterns for all the data from the period January 26, 1993 through July 31, 1995 (a duration of 2.5 years). The majority of the data from GOES 2 and GOES 3, and all of the data from ATS-3, were taken at fixed satellite longitude for each satellite. This majority configuration was: ATS-3 at ~105° W, GOES 2 at ~135° W, and GOES 3 at ~175° W. By far most of the observing hours were with GOES 2, with much less involving ATS-3 and only a few months (at the end of the 2.5-year period) involving GOES 3. Using the same event criteria as for Figure 4, but extending the exercise over the entire 2.5-year period, we show in Figure 5 azimuth distributions for all the data, separately for each of these three satellites. The gross azimuth diagreement between the sets of events recorded with GOES-2 and ATS-3 beacons confirms, with a very large

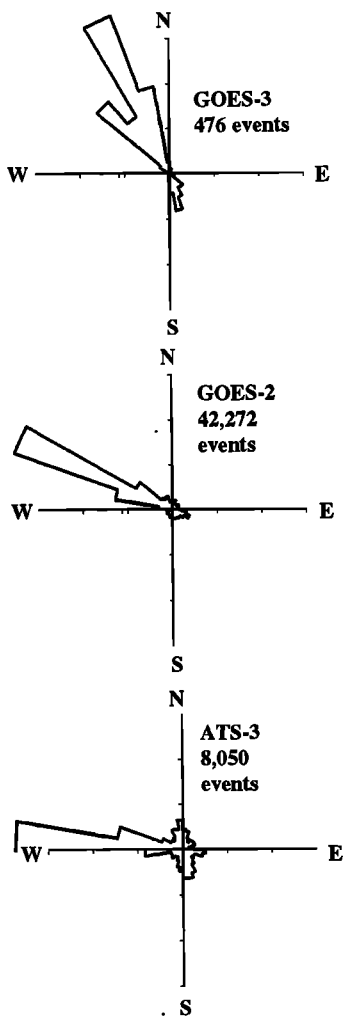

Figure 5. Polar plots of event-azimuth distributions for lines of sight to each of three satellites. The event selection criteria are explained in the text. The radius is proportional to histogram counts.

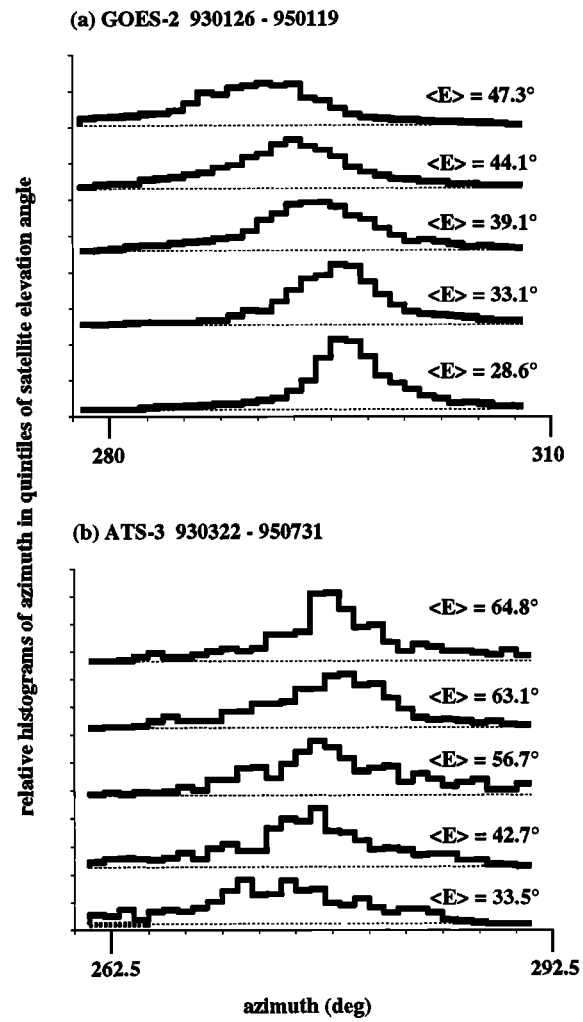

Figure 6. Event-azimuth distributions for lines of sight to (a) GOES 2 and (b) ATS-3, using selection criteria explained in the text. The data for each satellite are divided into quintiles of line-of-sight elevation, the mean of which (within each quintile) is indicated as "<E>."

statistical base, the same phenomenon already seen for one session's data in Figure 4 above. Furthermore, even the small data set with GOES 3, whose longitude has been even further west than those of the other satellites, indicates that the shift of the azimuth lobe clockwise, as the satellite is located further west, is a progressive phenomenon. Thus also in the case of the entire statistical data set, an interpretation of these TEC disturbances in terms of waves at ionospheric heights is rendered problematic by the anomalous azimuth behavior.

Finally, the variation of the event-azimuth distribution versus line-of-sight elevation provides further evidence of a remarkable anomaly. Each satellite oscillates between its extrema in latitude once per sidereal day. This enables us to sample the azimuth distribution for different line-of-sight elevation angles. Figure 6 shows the results of this for the period in which GOES 2 was at fixed longitude and for the entirety of ATS-3 (which was at fixed longitude always). The local time is restricted to the period 16 - 6 hours, a period during which most events are seen anyway (as explained below). These date and local time restrictions further restrict

the data set to ~17,000 events for GOES 2 and only ~2400 events for ATS-3. Figure 6 shows the resultant azimuth distributions over 30° domains near the peak for each satellite, within labeled quintiles of satellite elevation angle. Remarkably, the GOES 2 azimuth peak migrates counterclockwise as satellite elevation increases, while the ATS-3 azimuth peak (although noisier) migrates the other way. Also, the GOES 2 azimuth distributions become systematically broader as they migrate counterclockwise. This variation of azimuth versus line-of-sight elevation poses a particular challenge for any model of the shape and location of the irregularities.

4. Plasmasphere-Irregularity Hypothesis

In light of the VLA finding that plasmasphere irregularities accounted for most of the high-frequency disturbances seen with that instrument, and in light of the manifest problems of an ionospheric "phase screen" model in accounting for the behaviors shown in the previous section, we now consider a plasmasphere-irregularity model. Figure 7 shows two views of the plasmasphere, the top view a magnetic equatorial projection, and the lower view a magnetic meridian projection. On an L shell resides a zonally oscillatory irregularity, each of whose flutes is greatly extended along B within the shell. A

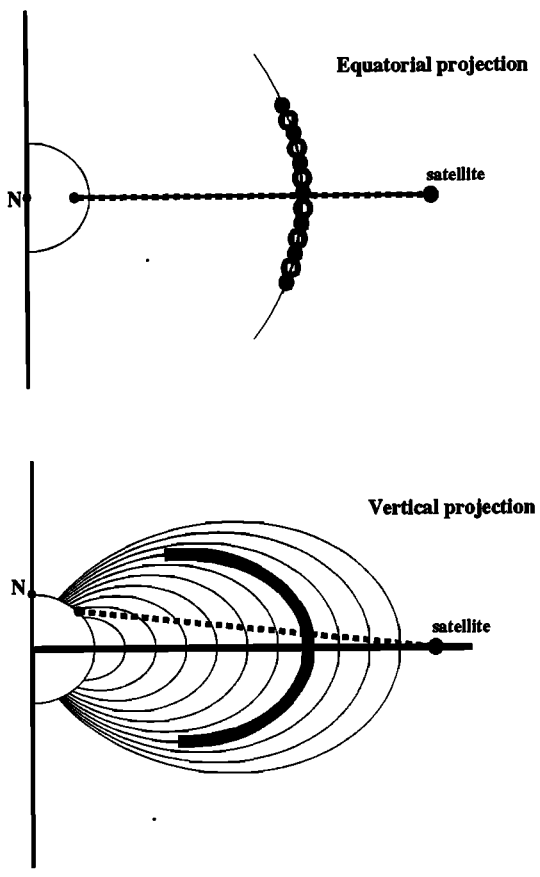

Figure 7. (top) Equatorial- and (bottom) vertical-projection views of a hypothetical zonally oscillatory irregularity in the plasmasphere. The structure consists of zonally alternating cells of overdensity and underdensity perturbations, each perturbation greatly extended along the geomagnetic field **B**. The line of sight is shown as a dashed line. "N" indicates the magnetic north pole.

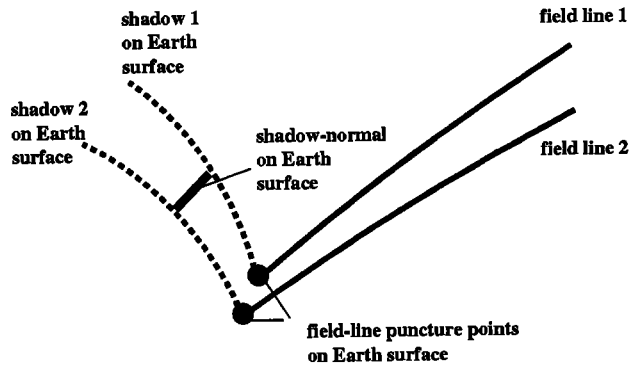

Figure 8. The "shadow concept:" Field lines (solid curves) are illuminated by spherical radio wavefronts from the satellite beacon. If the field lines were wires illuminated by light, they would cast shadows on the spherical surface of the Earth (dashed curves). In radio interferometry, there are still "shadows" (provided that the transverse scale exceeds the Fresnel scale), but they are in phase not amplitude. The normal (heavy solid line) to the shadows is the sole axis along which an interferometer (on the surface of the Earth) can sense shadow motion.

family of lines of sight from the satellite to the interferometer plane intersect the irregularity. The intersection of these lines of sight with that plane we will call the "shadow" pattern. In fact, the irregularites we will deal with are much larger than the transverse Fresnel scale, ensuring that geometrical optics is applicable; thus the shadow concept is valid. Figure 8 shows how the "shadows" are formed on the Earth surface. They are like optical shadows but are manifested in the phase not the amplitude. The shadows move across the Earth's surface to the extent that the causative irregularities move across the lines of sight. As this happens, the receivers at the interferometer stations discretely sample different parts of the drifting shadow pattern. The motion of the pattern may be resolved into two orthogonal components. The first component, along the shadows' own axis of elongation, produces no observable effect (at least over small geographical scales within which the shadows are sensibly straight and parallel to each other) and hence cannot be measured. The second component of shadow drift, perpendicular to the shadows' elongation axis, produces observable phase time variations at the receivers. This is the only component of drift which we can measure. Thus the azimuth of the "TEC disturbance trace velocity" is forcedly at right angles to the shadow and is completely determined by the projective geometry of a satellite beacon illuminating a geomagnetic flux tube and casting a phase shadow onto the surface of the Earth.

We can perform some simple but exigent tests of this irregularity-shadow hypothesis. To do so, we use a projective-geometry computer subroutine that represents the geomagnetic field as a centered but tilted dipole. We have compared the bearings of shadows obtained from both this simple dipole model and the *Tsyganenko* [1989] model for lines of sight to all our satellites and for irregularity positions everywhere in the range L=2 through L=3.6. For our three main satellites, namely ATS-3 (near the interferometer meridian) and both GOES 2 and GOES 3 (to the west of the interferometer meridian), the shadow-bearing discrepancies between the two geomagnetic field models were always < 1°. Since that is

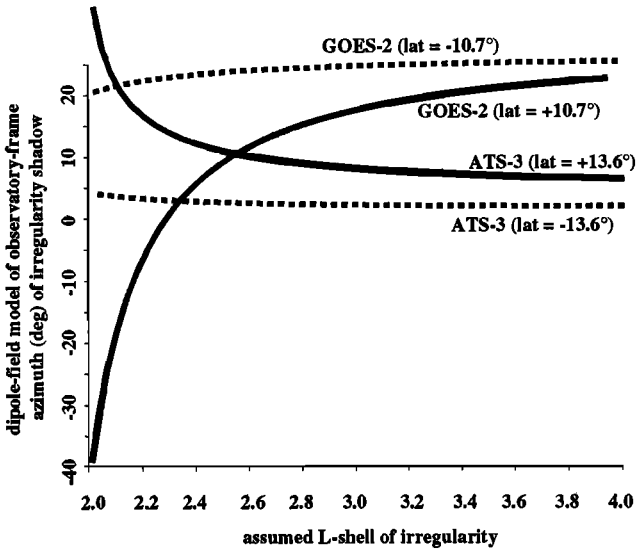

Figure 9. Tilted-dipole model of shadow bearing (at the Los Alamos array center) versus L shell, using lines of sight for both the high- and low-latitude extremes of GOES 2 and ATS-3. The GOES 2 longitude (~135°) used here describes GOES 2 prior to its move westward, which began on January 19, 1995.

sufficient for modeling the observed event azimuths (which themselves are measured with no better accuracy than 1°- 5°, depending on observing conditions), we use only the tilted-dipole model in what follows. However, for one drifting satellite (ATS-1), which was briefly observed, to the east of the interferometer, the discrepancy between the models can be quite bad, of the order of 10°. That is because the dipole model fails very badly for the inner plasmasphere in the South Atlantic Anomaly sector. For this reason data gathered with ATS-1 are used only in qualitative work but not in the statistical results later.

Test 1: Let us once again consider Figure 4. The sheath of straight lines accompanying each azimuth distribution comprises eleven shadows in the interferometer plane, for irregularity positions along the line of sight where L=2 through where L=3.6, in steps of ΔL = 0.16. That is, the shadows are generated by hypothesizing an irregularity at the given L shell, on the field line in the L shell where the line-of-sight punctures the L shell. Note that the shadows for a given satellite almost coincide in bearing and that their west normal aligns exactly with the azimuth lobe observed. The two satellites' anomalously different azimuth lobes in Figure 4 are exactly explained.

Test 2: Figure 9 shows the bearing of shadows versus irregularity position along the line of sight, for each latitude extreme for each of two satellites (valid for GOES 2 before January 19, 1995, and for ATS-3 always). The solid curves are the shadow bearings versus irregularity L for the satellites' high-latitude extremes; the dashed curves are for the low-latitude extremes. Note that for all L, the shadow bearing for high-latitude GOES 2 illumination is rotated counterclockwise compared to low-latitude GOES 2 illumination, and that for ATS-3, the trend is weaker but reversed in polarity. Noting that the west normal's azimuth is (by definition) always -90° with respect to the shadow bearing itself, similar trends are implicit for the west normals. Thus the behavior of the event azimuths versus satellite elevation angle, shown in Figure 6, is a natural fallout of the irregularity-shadow hypothesis.

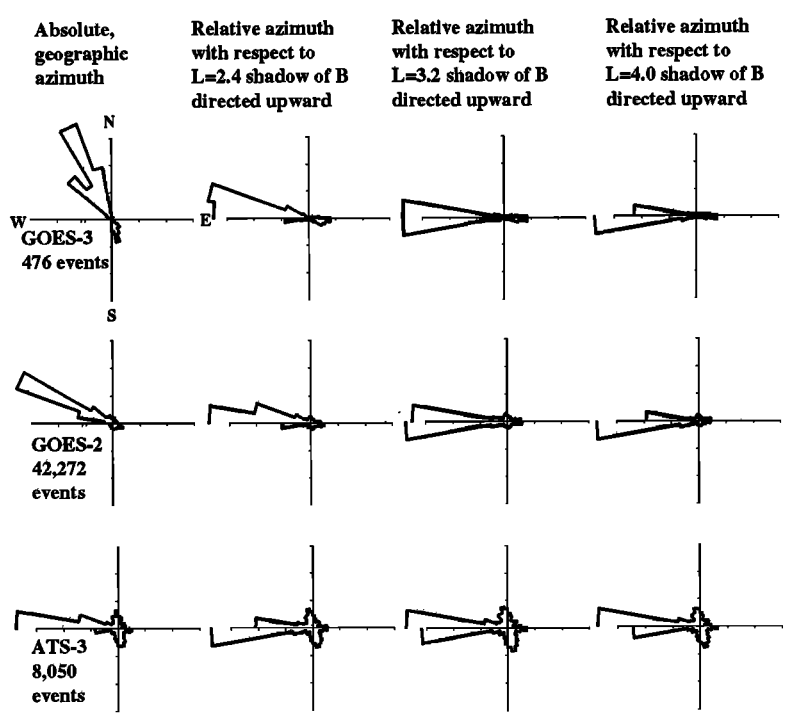

Figure 10. (left column) Polar plots of event azimuth distributions for lines of sight to each of three satellites, repeating the data of Figure 5 above. (other columns) Relative azimuth distributions, assuming irregularity locations at L=2.4, 3.2, and 4.0 respectively. The relative azimuth is the azimuth of the observed event, relative to the bearing of the shadow on the interferometer plane. Thus, if the event bearing were along the shadow's west normal, it would lie along the left horizontal axis in such a plot. The event selection criteria are explained in the text. The radius is proportional to histogram counts.

Test 3: Using all the data, and positing irregularity locations (along the instantaneous lines of sight) at three spaced L shells, we can explain the gross azimuth behavior quite well. Figure 10 shows the original geographic azimuth data (from Figure 5, above) in the left column, then transforms the same data into relative maps, in which the shadow is directed from down to up, and the west normal is directed therefore to the left. There is a separate column for each successive choice of L. Clearly, all three choices of L do quite well at reconciling the azimuth behavior of the leftmost column, but of the three choices, L=3.2 does sensibly better than do L=2.4 or L=4.0. (That is, if one had to assign a single effective L for this data set's events, one would be forced to choose L~3.2 over either 2.4 or 4.0. However, it will be seen later that we can do much better than to posit one, uniquely disturbed L shell.) Another obvious feature of Figure 10 is that most of the events are disposed along the west normal, some are disposed along the east normal, and (mainly for ATS-3) still a smaller set are totally unrelated to either normal.

There is a basic ambiguity regarding the irregularity-shadow hypothesis which must be lifted before we can start systematically exploiting the data to extract useful information about the irregularities themselves: We have shown that the shadow bearing, and hence the shadow-normal azimuth (toward which trace propagation is sensed), are uniquely determined modulo 180° by the position at which the irregularity lies on the line of sight. But the question remains, what direction of in situ irregularity drift is responsible for the drift of the shadows across the array? There are basically two choices, or some combination of the two. Consider the irregularity as aligned along **B**, that is, along the unit vector **b**. Let another unit vector **c** be the outward normal to the L shell, and let **a** = **bXc** be directed toward the in situ magnetic east direction. Then either perpendicular/outward (namely, along **c**) or zonal (namely, along **a**) in situ irregularity drift could in principle generate a trace velocity for the shadow in the irregularity plane. Fortunately, these two possibilites can be tested, and one can be rejected. Consider two satellites symmetrically separated in longitude from the interferometer meridian, one to the east, and the other to the west. If there is dominant in situ drift in the -**a** direction, that is, in the magnetic west direction, then the trace propagation azimuths in the interferometer plane would be along the shadow's west normal in either case. By contrast, if the dominant in situ drift were in the -**c** direction, that is, in the perpendicular/inward direction, then the trace azimuths for events seen with the west satellite would be along the shadow's west normal, while the trace azimuths for events seen with the east satellite would still be along the shadow's east normal. This difference can be applied as a test to the data. Figure 11 shows event azimuth lobes for GOES 2 (top) and for ATS-1 (bottom) for local times 16 - 02 hours during the period April 20 - June 30, 1994. At those times, the two satellites were approximately symetrically disposed to the west (GOES 2) and to the east (ATS-1) of the interferometer meridian. The drift of ATS-1 eastward during this period served to broaden its event azimuth lobe, but the basic logical impact of Figure 11 remains clear: The two satellites' event azimuth distributions are both along the respective shadows' west normals, even though the satellites lie on opposite sides of the interferometer merdidian, so the causative in situ drift must be zonal, not meridional.

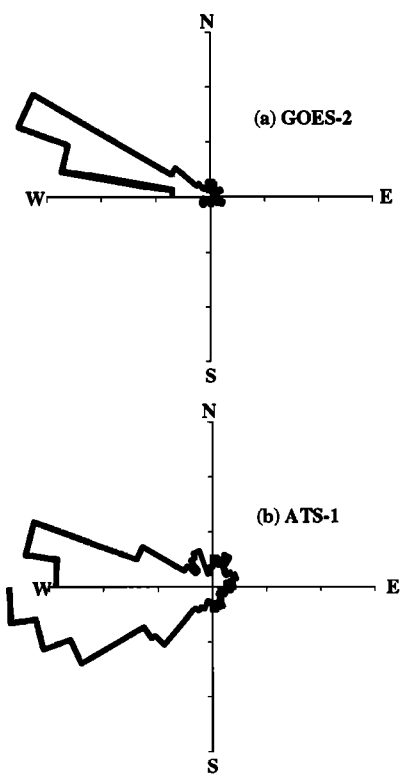

Figure 11. Polar plots of event azimuth distributions for lines of sight to (a) GOES 2 and (b) ATS-1, during the period April 20 to June 30, 1994, and between local times 16-02 hours. GOES 2 was on the west of the interferometer, while ATS-1 was on the east. The event selection criteria are explained in the text. The radius is proportional to histogram counts.

We caution that the above argument for an **a**- rather than **c**-directed origin of the observed trace drifts is borne-out for the high-frequency ($f \geq 3.1$ mHz) data treated here but is not true in other cases: For lower frequencies ($f < 3$ mHz), the situation is less clear, so consideration of those lower frequencies will be deferred to a future publication. Indeed, our present restriction to high frequencies ($f > 3.0$ mHz) is required in order to be able to interpret the trace velocities in terms of in situ zonal drift.

5. Non-L-Resolved Properties of the Observed Irregularities

We are now in a position to accept the plasmasphere-irregularity model and to extract from the data some statistical information about the irregularities and their motion. To do this, we will posit that if the irregularities are to be considered at some "typical effective L shell"; L~3.2 is an optimum choice (see Figure 10 above). In this section, we calculate for each observation epoch the bearing of the shadow of an irregularity at L=3.2 along that epoch's instantaneous line of sight, and then accept all events with ±20° of either the east normal or the west normal of that shadow. The dates used are January 26, 1993 to July 31, 1995; the three satellites used are GOES 2, GOES 3, and ATS-3. Figure 12 shows the local time probability (i.e., events found per observation epoch), for the west normal (top) and for the east normal (bottom) separately. In each graph the half-year periods centered on winter and summer solstices are shown as solid and dashed curves respectively. (The top and bottom panels do not use the same ordinate scale). The first thing to note from Figure 12 is that

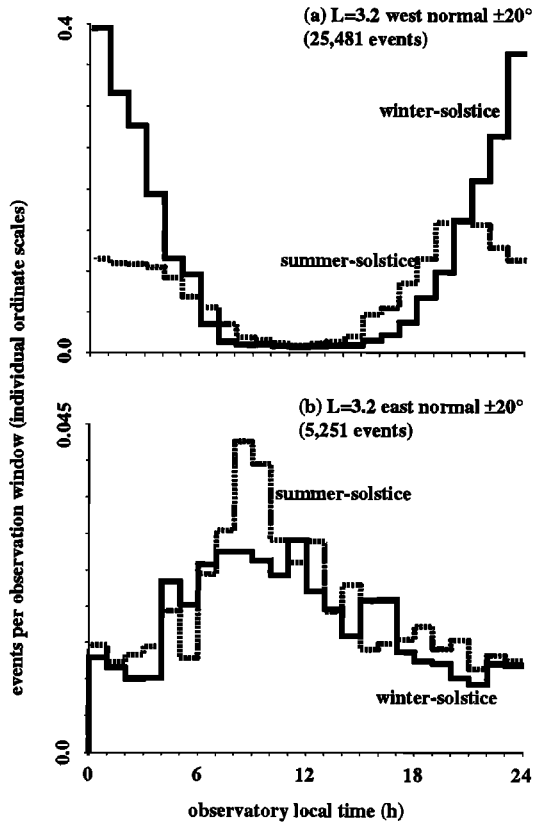

Figure 12. Local time dependence of probability of (a) west-normal and (b) east-normal events, for half-years centered on winter solstice (solid) and on summer solstice (dashed). The event-selection criteria are explained in the text.

there is a remarkable complementarity in the local time probabilities of the east and west normals' subpopulations. The west-normal events peak during the night (midnight in winter, and evening in summer), while the east-normal events peak during the forenoon. There is a practically complete absence of west-normal events around midday. The seasonal modulations are also roughly complementary: During summer the east-normal events' max/min contrast is enhanced, whereas during winter the west-normal events' contrast is enhanced. The majority type of event being west-normal, it follows that the irregularities we see are primarily centered on nighttime. This fact suggests that a key role may be played by either (1) a magnetospheric driver (from the tailward, antisunward side of the magnetosphere) or (2) a requisite ionospheric condition (suppressed Pedersen conductance during nighttime).

The probability of events of either polarity is enhanced by magnetically disturbed conditions, as shown in Figure 13 for the same subpopulations of west-normal (top) and east-normal (bottom) events. The most disturbed bin (i.e., the rightmost) represents only <3% of the observing windows and is thus not statistically as signficant as are the other bins. Nonetheless, it is clear from Figure 13 that both west- and east-normal events are more probable during high-K_p epochs.

To explore the K_p effect on the events in more detail, we divide observed events into quartiles of K_p. Figure 14 shows rms TEC-perturbation-amplitude distributions for west-normal (top) and east-normal (bottom) events. The solid curves are for the geomagnetically most quiet, and the dashed curves for the most disturbed, quartiles. The first thing to notice is that the TEC perturbations are stronger for the west- than for the east-normal events, independent of K_p. The second thing to notice in Figure 14 is that TEC-perturbation amplitudes are enhanced by magnetic disturbances, for either polarity of drift. The fact that west-normal events predominantly occur during the nighttime, while east-normal events predominantly occur during the daytime (see Figure 12 above), implies that nighttime is thus the time of more intense irregularities, as well as of more numerous ones. This reinforces the notion that a key role may be played by either (1) a magnetospheric driver (from the tailward, antisunward side of the magnetosphere) or (2) a requisite ionospheric condition (suppressed Pedersen conductance during nighttime).

Figure 15 repeats the quartile exercise, but this time for event trace speed. (The quantitative interpretation of trace speed will be discussed later.) We see that high K_p causes elevated traces speeds for west-normal events but that for east-normal events the effect is less clear.

6. L-Resolved Properties of the Observed Irregularities

It will be recalled (see Figure 9, above) that for any given line of sight, the shadow bearing varies monotonically with where, along the line of sight, the irregularity is located. If the interferometer could make perfect measurements of shadow bearing, then we would be able to infer the L shell of the irregularity arbitrarily well.

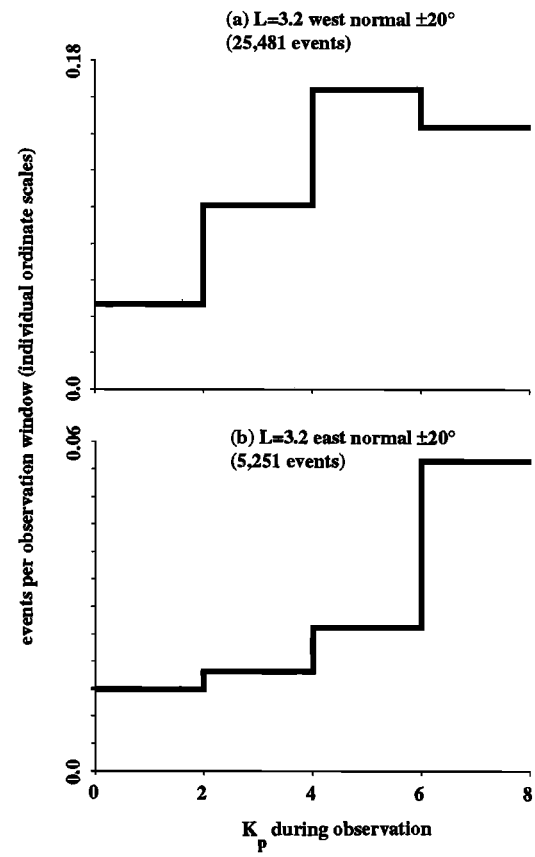

Figure 13. K_p dependence of probability of (a) west- and (b) east-normal events. The event-selection criteria are explained in the text.

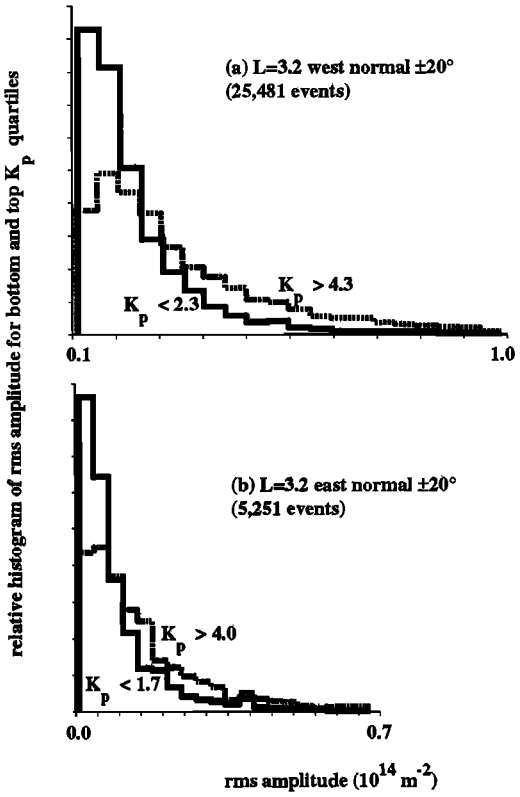

Figure 14. Rms-amplitude distributions for (a) west- and (b) east-normal events. Only the lowest- (solid) and highest-K_p (dashed) quartiles are shown. The event-selection criteria are explained in the text.

In practice, measurement uncertainties at this stage in the interferometer development appear to impose a measured-azimuth rms uncertainty of the order of ~5° or so. To establish this fact, we have exploited a feature of the predicted shadow-bearing which is apparent from Figure 9 above: Most of the sensitivity of the bearing-as-a-function-of-L relationship is at the low-L end of the range. The higher-L end (L>3.0) is relatively insensitive. For L ~ 4.0, the bearing-as-a-function-of-L relationship is essentially saturated and of no value for this project, other than saying that an irregularity resides at L>3 rather than at, say, L=2.1. Notice (see Figure 9 above) that there is effectively a firewall of possible predicted shadow bearings: The L=4 predicted bearing is within 1 deg of the maximum bearing we should expect to see with the GOES 2 beacon, and the L=4 predicted bearing is within 1 deg of the minimum bearing we should expect to see with the ATS-3 beacon. This natural "firewall" allows a realistic assessment of the azimuth accuracy of the interferometric measurement of refractive irregularities. The spillover of the measured azimuth distributions, past the respective L=4 firewalls for the two satellites GOES 2 and ATS-3, reveals the worst-case "instrumental" uncertainty in determining azimuth. Figure 16 shows the azimuth distributions relative to the predicted L=4 shadow's left normal, for GOES 2 (Figure 16a) and ATS-3 (Figure 16b), within +/- 40° of relative azimuth. In this relative-azimuth range there are 24,659 accepted events for GOES 2 and 3434 accepted events for ATS-3. The first thing to note is that there is a quasi-isotropic baseline. This is relatively more important for ATS-3, where there are fewer events in the peak. The second thing to note is that the spillover to the wrong (marked by a cross) side of the L=4 bearing has a 1/e width of around 5°. Thus we must conclude that the azimuth-measurement uncertainty may be no better than +/- 5°.

The implication of this +/- 5° is that we can, at this point in the interferometer development, make only semiquantitative statements about the L location of an irregularity. For example, with a line of sight whose bearing-as-a-function-of-L relationship is relatively sensitive, we can certainly differentiate between an irregularity's being at L=2.1 and its being at L=4.0, but we cannot tell the difference between L=3.4 and L=4.0. With a line of sight whose bearing-as-a-function-of-L relationship is relatively insensitive, we can tell nothing about the L-location of the causative irregularity.

Incidentally, Figure 4 (above) is an example of two very L-insensitive lines of sight. The ATS-3 line of sight is intrinsically insensitive, and the GOES 2 line of sight in this instance is toward the satellite at its low-latitude extreme. Consequently, each sheath of irregularity shadows in Figure 4 is only weakly dispersed in angle.

By contrast, the data in Figure 2 (above) was taken with GOES 2 relatively high (8.6°) in its latitude range, and the line of sight is very L-sensitive. Figure 17 (top) shows the appearance on the interferometer plane of eleven shadows (spaced by ΔL = 0.16, from L=2.0 to L=3.6) for this line of sight. Figure 17 (bottom) also shows the shadow bearing versus L more quantitatively. It is clear that the measurement error (~5°; see discussion above) would permit inferring L with a resolution ΔL < 0.1 for irregularities at L < ~2.5, but only more crudely farther out. More sensitive lines of sight are now

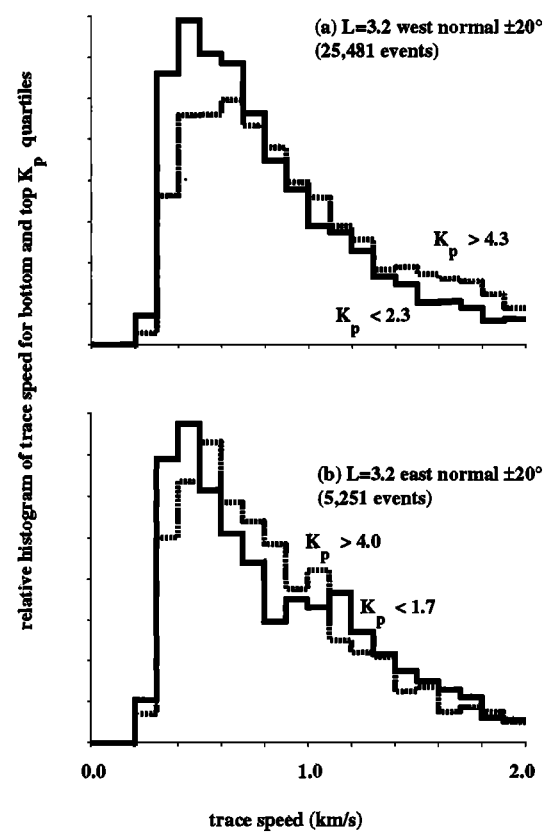

Figure 15. Similar to Figure 14, but showing trace-speed distributions.

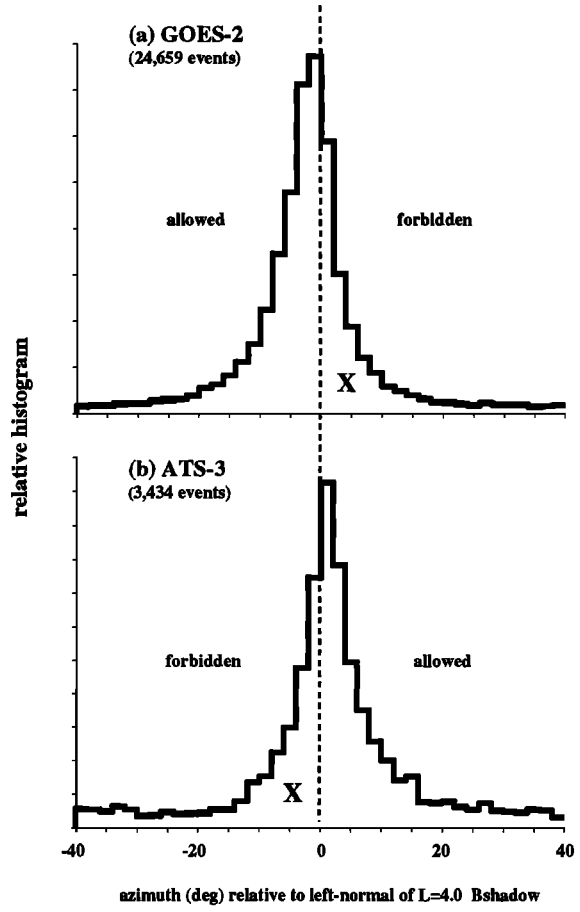

Figure 16. Histogram of event azimuth relative to left normal of L=4.0 shadow. (a) GOES 2 (24,659 events); (b) ATS-3 (3434 events). The cross marks those sides of the L=4 shadow normal which are not theoretically possible for any L value. The spillover into these zones is an indicator of the errors made in determining propagation azimuth with the current technique.

available (e.g., on the west-shifted GOES 2 longitude available in spring 1995), but this example serves to illustrate the trend: The best resolution in L occurs when the irregularity is in the inner plasmasphere, whereas further out the resolution degrades and eventually becomes not useful at all. For the two peaks indicated at the bottom of Figure 2 (above), the inferred irregularity L shell is the same, namely L~2.1.

Thus we see that for suitably "sensitive" lines of sight, and especially for inner plasmasphere irregularities, the event azimuth allows us to infer from the measurement itself the L shell of the causative plasmaspheric irregularity. With such lines of sight, we can much more completely exploit the interferometer data to learn about the irregularities per se. The following discussion will highlight some results; the reader interested in mechanical details should consult the appendix.

The 256-sample (37-min) window shown in Figure 2 (above) is part of a longer (several-h) episode of quasi-continuous west-normal activity. Figure 18 (top) shows baseline phases versus time for a 3-hour duration. Figure 18 (bottom) shows irregularity properties inferred from measured quantities. There is one data point for each inferred property of each event. The vertical dashed line is through the center of the 256-sample window shown earlier (see Figure 2 above). First, the bearing alone allows inference of where, along the line of sight, the irregularity lies. This is shown to lie at L~2.0-2.2, corresponding to altitudes of 0.5 - 0.9 R_E for the duration of the high-frequency activity. Second (see the appendix), combining this location inference with the measured trace speed allows one to map the drift down along the flux tube to the F layer and state a zonal drift speed there. The lowermost points in Figure 18 (bottom) show that the L~2.1 mapped F layer magnetic westward drifts are in the range 60 -110 m/s for these events.

Having ascertained that some lines of sight are usefully L sensitive, we define a sensitivity threshhold for further downselection of observed events in order to choose the most sensitive lines of sight: We will require of a given line of sight in what follows that between L=2.0 and L=3.6 the cumulative shadow-bearing rotation exceed 20°. This immediately eliminates all ATS-3 data and retains only portions of GOES 2 and GOES 3 observing time. Next, of each event whose instantaneous line of sight satisfies this requirement, we further require that the inferred L shell is in the range 2.0 - 3.6. This downselection results in only 10,783 retained west-normal events and only 2,056 retained east-normal events, that is, only ~40% as many events as used in Figures 12-15 above.

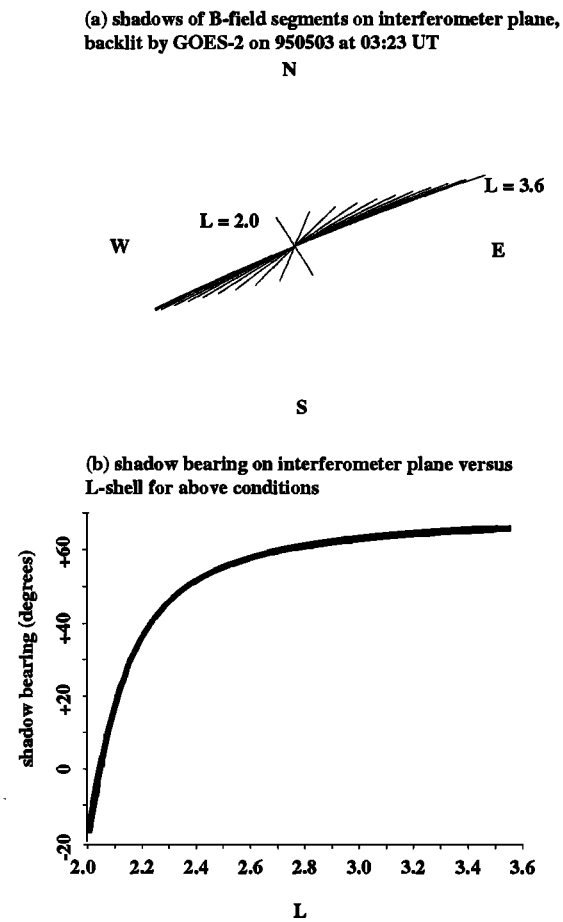

Figure 17. (a) Shadows on interferometer plane corresponding to eleven L shells, equally spaced in the range L=2 to L=3.6, for line of sight to GOES 2 at 0323 UT on May 3, 1995 (the epoch of Figure 2 above). (b) Shadow bearing versus L shell for the same line of sight.

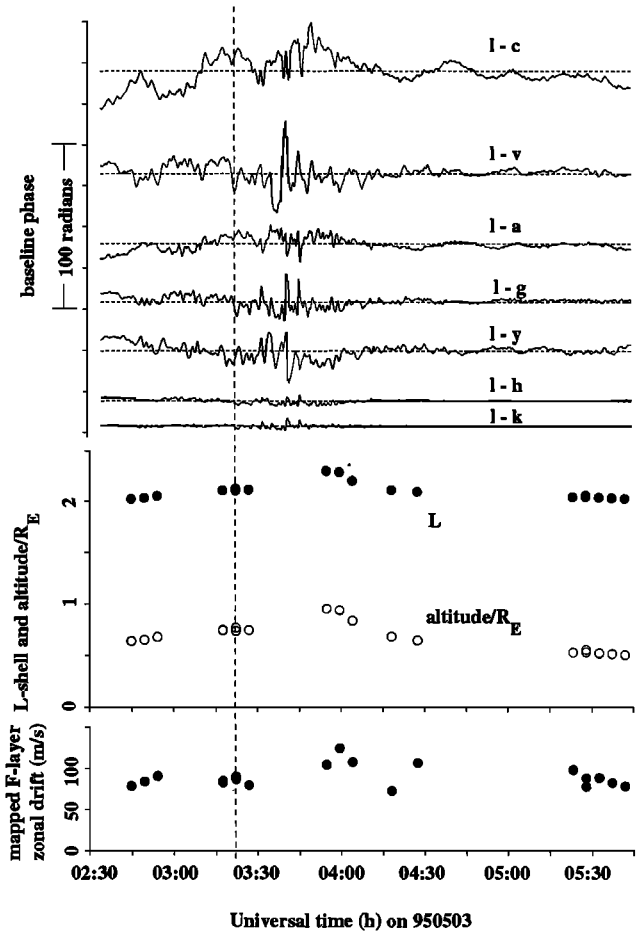

Figure 18. (top) Baseline-phase versus time for a period in which the shorter-duration data of Figure 2 are centered at the dashed vertical line. (bottom) Inferred L shell, altitude, and mapped F-layer zonal drifts for the events from this epoch. The overlapping pair of points indicated by the vertical dashed line correspond to the two spectral peaks in the bottom of Figure 2.

Now that the data are being used to infer L resolved quantities, we repeat the caveat regarding our drift-direction assumption: We have assumed that the causative irregularity drifts are in the magnetic zonal direction. For this frequency range ($f > 3$ mHz) this assumption is statistically supported by (1) the comparison between data from GOES 2 and ATS-1 and (2) the very fact that ATS-3 (which is nearly in the Los Alamos magnetic meridian) sees these events at all. However, it is to be remembered that this confirmation of our assumption is only statistical, and that there could be admixed, into our data set, events whose irregularity drifts are substantially across the L shell.

Figure 19 shows the L distribution of downselected west-normal (top) and east-normal (bottom) events. The west-normal events are most likely to be seen at moderate L (~2.4 - 3.2), while the east-normal events are crowded toward the inner boundary (L=2.0) of the L distribution.

Figure 20 shows the inferred magnetic-zonal angular wavelength for west- (solid curve) and east-normal (dashed curve) events. This distribution peaks in either case for the range ~4-8 milliradians, corresponding to "poloidal mode numbers" of the order of 10^3. Two cautions are in order: First, we see no evidence of globally coherent "modes," so the use of "mode number" is just a shorthand for denoting the zonal angular period of the disturbances. Second, the event criterion that the trace wavelength $\lambda_t > 75$ km biases what events are counted, in such a way as to vignette the distribution's left end in Figure 20. We note that half-as-large angular wavelengths had been seen with the VLA [*Jacobson and Erickson*, 1993; *Hoogeveen and Jacobson*, 1995), which did not require the constraint $\lambda_t > 75$ km.

The one place along the field line where an absolute-distance zonal wavelength (as opposed to an angular zonal wavelength) might be meaningful is at the F layer "footprint" of the field line (see the appendix for details of its derivation). Figure 21 shows this F layer wavelength distribution for west- (solid curve) and east-normal (dashed curve) events. The distributions' peaks are in the range ~15-30 km and thus are too low to correspond to common thermospheric gravity waves. If anything, the observing bias introduced by trace wavelength skews this distribution toward longer scales than might be true of the irregularities themselves seen with an unbiased instrument. It is perhaps noteworthy that this range of zonal cyclical wavelengths is comparable to the cross-L thickness of whistler ducts inferred by satellite flythroughs [*Angerami*, 1970].

7. Discussion

The characteristics of lowlatitutude to midlatitude ionospheric electric fields have been studied extensively with incoherent scatter radar observations of F region electrodynamic plasma drifts at Arecibo (L=1.3) [*Gonzales et*

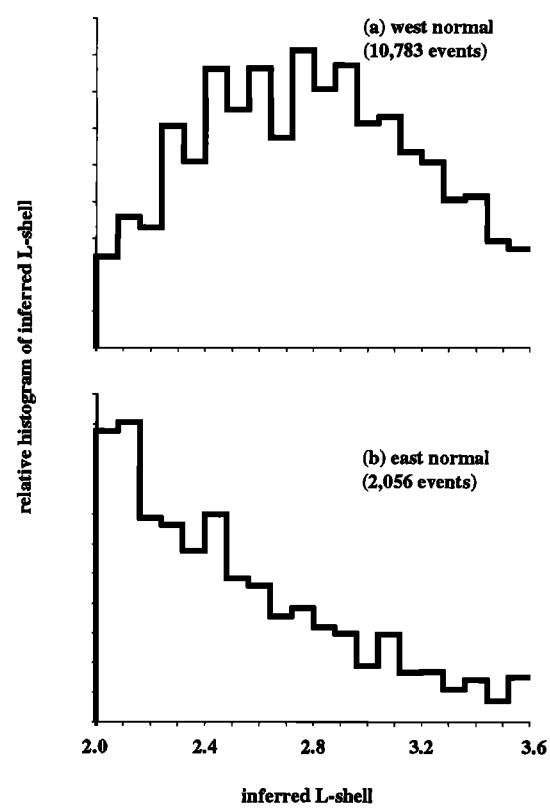

Figure 19. Inferred L shell distributions for (a) west- and (b) east-normal events. The event-selection criteria are explained in the text.

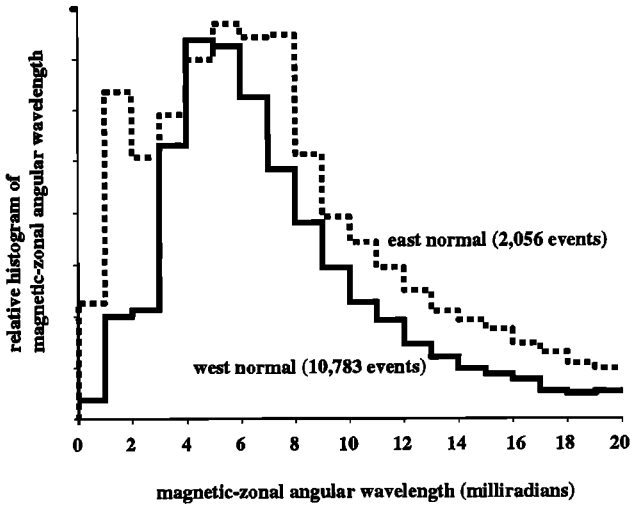

Figure 20. Magnetic zonal angular wavelength distributions for west- (solid) and east-normal (dashed) events. The event-selection criteria are explained in the text.

al., 1983; *Ganguly et al.*, 1987; *Fejer*, 1993], Shigaraki (L=1.3) [*Oliver et al.*, 1993], Saint-Santin (L=1.8) [*Blanc*, 1983], and Millstone Hill (L=3.2) [*Wand*, 1981; *Wand and Evans* 1981; *Yeh et al.*, 1991; *Buonsanto and Foster*, 1992; *Buonsanto et al.*, 1993], and also with satellite observations [*Heelis and Coley*, 1992]. These measurements have determined the average plasma drift patterns during magnetically quiet and disturbed conditions and have also shown the occurrence of complex plasma drift (electric field) patterns in response to high-latitude current disturbances. The storm time plasma drift perturbations (electric fields) result from short-lived (time constants of about an hour) direct penetration of high-latitude electric fields to lower latitudes and from longer-lasting (about a few hours) ionospheric storm time dynamo effects. At upper midlatitudes, the plasma convection patterns can also be disturbed by the equatorward expansion of high-latitude current systems. The average zonal disturbance electric fields (perpendicular/upward plasma drifts) are very small below about L~2. At higher latitudes they are westward (corresponding to perpendicular/downward drifts) between midnight and noon and eastward at later times [*Wand*, 1981]. Disturbance effects are significantly larger on the meridonal electric fields (zonal drifts), which are the component to which the present data set pertains. The average disturbance zonal drifts are westward at all local times from equatorial to lower midlatitudes, with largest speeds in the postmidnight sector. At higher midlatitudes, the westward disturbance drifts occur at earlier local times, maximizing in the afternoon-dusk sector at invariant latitudes of about 50° - 60°. In this case, the morning-noon drifts are eastward [*Wand*, 1981; *Heelis and Coley*, 1992]. It should be kept in mind, however, that on individual days the measured drifts exhibit significant departures from the average patterns, and that they depend strongly on the characteristics of the high-latitude forcing as well as on storm time [*Fejer and Scherliess*, 1995].

Clearly, the bulk of our observed events occur on L shells closer to Millstone Hill (L=3.2) than to the other midlatitude observatories. Therefore the following remarks make a very broad-brush comparison of our data's evidence concerning zonal drifts and the corresponding drift climatology established for Millstone Hill. However, it is important to bear in mind that our dataset is as yet too small and too biased to allow us to make detailed statements about drift climatology. Indeed, the very condition for drift visibility in our diagnostic approach, that there be suitable plasmaspheric irregularities, is something which imposes an immediate bias on our technique. In other words, the interferometric technique of zonal-flow inference depends on another feature of geomagnetic disturbance, namely, the existence of suitable field-aligned irregularities, which might depend in a complicated manner (of which we are ignorant) on the recent and current electrodynamic/aeronomic forcing of the plasmasphere.

The pattern in our data of westward drifts peaking in evening/night, and eastward drifts peaking in forenoon/midday (see Figure 12), are broadly compatible with that which is seen at Millstone Hill.

We turn now to the origin of the plasmaspheric irregularities themselves. Most researches view the plasmasphere as a cold, relatively dense, featureless region corotating with the Earth. This notion is put in question by the existence of whistler ducts, however, which have long since been well established as a necessary condition for the guidance of VLF electromagnetic waves between the hemispheres. Likewise, at least near the plasmapause, it has long been known that "pieces" of the high-latitude ionosphere/magnetosphere can apparently be observed inside the plasmasphere.

More recently, the equatorward edge of the diffuse aurora has been found sometimes to exhibit curious ripples and cusplike features when viewed from space [*Lui et al.*, 1982] and from the ground [*Mendillo et al.*, 1989]. *Kelley* [1986] pointed out that this same region on occasion is co-located with a high-velocity, narrow (in latitude) plasma jet driven by an intense poleward electric field [*Smiddy et al.*, 1977; *Spiro et al.*, 1978]. The total potential across this region is about 25 keV, and ionospheric flows as high as 9 km/s (300 mV/m E field) have been reported. *Kelley* [1986] also suggested that this sheared flow pattern might be responsible for the undulations of the diffuse auroral boundary via a Kelvin-Helmholtz instability, and computer simulations of this process have

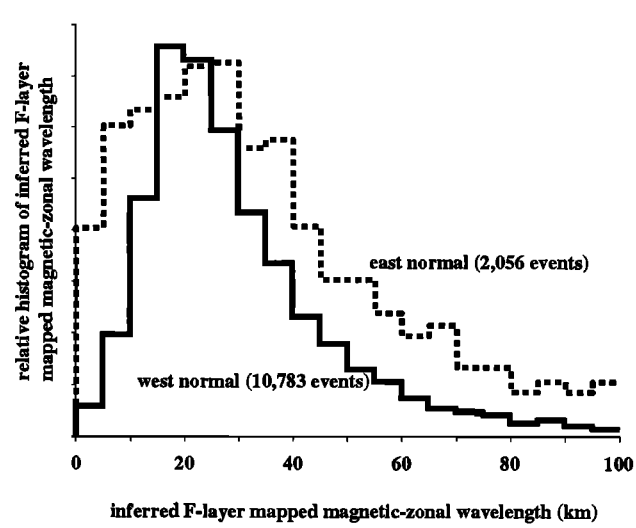

Figure 21. Inferred F layer magnetic zonal mapped wavelength distributions for west- (solid) and east-normal (dashed) events. The event-selection criteria are explained in the text.

been reported which support the notion [*Yamamoto et al.*, 1991, 1994]. The ripples are observed to have characteristic scales the order of 400 km as measured at ionospheric heights, however, which is an order of magnitude larger than the irregularities reported here. Furthermore, the plasma jet is sporadic, possibly related to magnetic storms or substorms.

In addition, even without these storm-related processes, at least the outer plasmasphere has several features conducive to irregularity formation. First, there is the plasmaspheric gradient itself. Any turbulence at all in the flow field will mix this gradient and create plasma structure. Second, there are two sources of shear in the outer plasmaspheric flow. One is the transition between the first-order corotation of the inner region and the convection of the solar-wind-controlled auroral zone. Less well known is the fact that a shear exists in the corotating frame.

Except for the Kelvin Helmholtz studies mentioned above, as well as work by *Vinas and Madden* [1986], *Richmond* [1973], and *Huang et al.* [1990], plasma instability studies of this region have not been particularly successful in providing in situ explanations for what now seems to be a fairly common occurrence of structure. Ionospheric sources for the plasmaspheric structure are also problematic. *Park and Helliwell* [1971] proposed that thunderstorm cells could create vortical flows in the ionosphere which mix the entire flux tube. Rocket flights over thunderstorms [*Kelley et al.*, 1986, 1990] have verified intense wave electric fields but have not provided evidence for quasi-dc fields at ionospheric heights. Ionospheric plasma processes may provide a source of structure in the plasmasphere, since it is now fairly well established that mesoscale electric fields accompany certain classes of gravity-wave ionospheric interaction. Remote sensing devices such as the Arecibo and MU radars have reported 200-400 m/s flow fields at the 50-200 km scale. Such electric fields must map throughout the flux tube, and indeed have been detected on the AE spacecraft [*Hanson and Johnson*, 1992] and on Viking [Baumjohann, personal communication, 1995]. In the presence of a gradient these highly structured electric fields may well mix or seed the plasmaspheric response.

Turning to in situ observations, we find very little data in the literature concerning the structure of the plasmasphere above about 1000 km. That is, although we have considerable knowledge concerning ionospheric irregularities, the plasmasphere is more difficult, since particle detectors usually do not measure the thermal particles, and Langmuir probes have not been very successful there. The plasma-wave receiver on the CRRES satellite, however, has had some recent success in measuring the plasma density and its fluctuations [*LeDocq et al.*, 1994]. They find that the plasmasphere is indeed irregular, particularly near the plasmapause, and have published some examples of the power spectra measured in the moving spacecraft frame of reference. Since these are the only quantitative measurements available, it is appropriate to compare them with those reported here.

To make such a comparison is not trivial, and we have proceeded as follows: We first convert the LeDocq et al. frequency spectrum into a k spectrum, under the hypothesis that the irregularities move much more slowly than the satellite. For convenience we take the satellite velocity to be 2π km/s and thus avoid scale modification in the LeDoc et al. plot if the units are simply changed to radians per kilometers on the ordinate and cm^{-6} km on the abscissa. To place the present observations in this context we need to generate a spectral density as well. The scales at plasmaspheric heights of the irregularities presented here correspond to the range 10 km $< l <$ 100 km. At this point in our study we do not have any idea about the form of the spectrum in this range since the Ledocq et al. spectrum ends at about this range. For an estimate a power law is probably reasonable. *Ledocq et al.* [1994] report a -5/3 law for their spectrum, which is valid for $60 < l < 1000$ km, and most geophysical processes have power law spectra with indices in the range -1 to -3. If we take -2 as a typical value, then the broadband δn values inferrable from our data using a simple round-cross-section irregularity model [*Jacobson and Erickson*, 1993] can be related to the spectral density at some k_0, using as a spectral density ~ $(\delta n)^2/k_0$. A simple exercise (see appendix and derivation of A4 which describes both uv-plane foreshortening and demagnification) on the accepted events allows us to infer that the in situ electron density perturbation amplitudes are in the range 10^7 $m^{-3} < \delta n < 10^8$ m^{-3} and a similarly broad range of in situ wavenumbers. Since we have a range of possible values for k_0 and for δn (e.g., 10^7 $m^{-3} < \delta n < 10^8$ m^{-3}), we can only indicate a two-dimensional block of possible spectral densities consistent with the present observation set and the power law hypothesis. These are shown superposed on the *LeDocq et al.* [1994] plot in Figure 22.

We see that our remote sensing data are consistent with the in situ measurement. If they are indeed related, the implication would seem to be that the dominant process lies at the larger scales, since the power spectrum peaks at a larger scale than the one to which our instrument is sensitive. However, in two-dimensional turbulence theory there is an inverse cascade of energy predicted with a 5/3 power law at scales larger than the energy input scale [*Kraichnan*, 1967; *Kintner and Seyler*, 1985]. Thus there could be an input scale below 100 km, and the same experimental results would pertain. At this juncture we are not prepared to speculate further on the inverse cascade idea, but a possible stirring scale in the appropriate range could be the steepened edges of ionospheric structures [*Miller*, 1996].

We can also speculate on the possibility of energy injection at the several-hundred-kilometer scale. We are

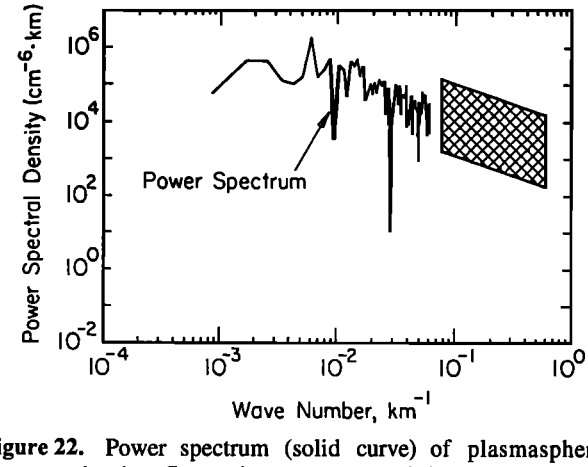

Figure 22. Power spectrum (solid curve) of plasmaspheric electron density fluctuations as reported by *LeDocq et al.* [1994]. The cross-hatched region indicates the estimated spectral density inferred from our measurements (see text for explanation).

reminded of the phenomenon of cold- and hot-core eddies in the Atlantic Ocean which are spawned by the Gulf Stream. Suppose that shear-induced undulations of the diffuse aurora are related to eddies of the same scale which are entrained in the plasmasphere. In effect pieces of the hot, low-density magnetosphere are spun off into the plasmasphere where they exist until the energy is dissipated.

How do our results on perturbation morphology agree with inferences made by VLF means on whistler ducts? First, the classic work with OGO 3 flythroughs of ducts [*Angerami*, 1970] established the cross-L width to be tens of kilometers (mapped to the F layer) but could not directly address the issue of zonal width. The data from satellite flythroughs tends to be silent about the zonal direction duct morphology simply because the path of a highly elliptical orbit cutting through the inner plasmasphere is dominantly radial. *Angerami* [1970] discussed zonal morphology only on the basis of the effective direction-of-arrival to ground-based VLF receivers. Moreover, it is not clear that ground-based VLF direction-finding techniques could distinguish between (1) one very zonally wide duct (as guessed-at in Figure 11 of *Angerami* [1970] and (2) the morphology we see with both the Los Alamos interferometer and the VLA [*Jacobson and Erickson*, 1993], namely of zonally oscillatory structures with alternate overdensities and underdensities. It is to be hoped that modern matched-filter approaches to reduction of whistler spectrograms [*Hamar et al.*, 1990] will eventually illuminate this issue of zonal structure. Better knowledge of the shape and cross-sectional area of whistler ducts would improve estimates of the radiation-belt loss budget due to precipitation events [*Burgess and Inan*, 1993].

Another means of improving our knowledge of whistler duct morphology would be with VLF instruments on board satellites in circular orbits with low orbital inclination, in the inner plasmasphere (geocentric radii ~ 2-3 R_E). The low inclination would ensure that the satellite track would sample the alternate overdensitites and underdensities of the perturbations seen with ground-based interferometers. To date, VLF-instrumented satellites, like COSMOS 1809 [*Sonwalker et al.*, 1994] are high inclination and hence are not suitable for sampling this zonally oscillatory variation of duct parameters.

An underlying difficulty in understanding the origin of the irregularities seen by our interferometer observations, which irregularities are presumably though not necessarily related to whistler ducts, is that ongoing work on plasmasphere dynamics [e.g., *Carpenter et al.*, 1993] tends to concentrate on the plasmasphere's radially outer boundary, which is most subject to change during shifts in magnetic disturbance level. However, it is clear from the L distribution of either whistler ducts or the interferometrically observed irregularities (see Figure 19 above) that the causative mechanism must be capable of acting far interior of the plasmasphere "boundary."

An outstanding research challenge is to account for the origin and zonally oscillatory behavior of the irregularities seen with interferometers and to establish their relationship to whistler ducts.

Appendix

This appendix explains the geometrical transformations used in the data analysis to infer (from the interferometer plane, or "trace," parameters) useful information about the plasmaspheric irregularities themselves. We will consider the complete series of steps, from interferometer plane measurements, to inferences about plasma drift.

A1. Transformation Between Interferometer Plane and Normal Plane

The interferometer (or "trace") plane is tangent to the spherical surface of the Earth and contains the interferometer stations. This plane contains local geographic directions E, S, W, and N. Figure A1 shows the interferometer plane from the view of an observer above and to the NW of the plane. The line-of-sight unit vector $\hat{\mathbf{u}}$ defines a plane normal to itself, the "normal plane" (called by radioastronomers the "uv plane"). The line of sight is elevated by an angle β above the interferometer plane. The horizontal projection of $\hat{\mathbf{u}}$ in the interferometer plane is at local azimuth α clockwise from N.

The transformation of trace velocity $\mathbf{V}_t$ into normal-plane velocity $\mathbf{V}_n$ is as follows: In the interferometer plane, decompose $\mathbf{V}_t$ into a component $\mathbf{V}_{t1}$ parallel to, and a component $\mathbf{V}_{t2}$ perpendicular to, the local vertical plane ABC containing $\hat{\mathbf{u}}$. Use the intersection line of this vertical plane containing ABC with the normal plane to define direction 1 in the normal plane. Direction 2 in the normal plane is perpendicular to direction 1 in the normal plane and coincides with the interferometer-plane direction 2. We obtain

$$V_{n1} = V_{t1} \sin \beta \tag{A1}$$

$$V_{n2} = V_{t2} \tag{A2}$$

Equations (A1) and (A2) express the anisotropic foreshortening of interferometer plane spatial scales into the normal plane. Thus trace velocities must tend to exceed normal-plane velocities, and for low elevation angle lines of sight, the effect can be dramatic. Figure A2 shows this for the simple case of a linear interferometer array all of whose stations are in the vertical plane containing the line of sight. In this case the trace wavelength λ_t is forcedly longer than the normal-plane wavelength λ_n. Since frequency is unchanged by the transformation, we expect speed and wavelength to each to scale in the same way from trace plane to normal plane.

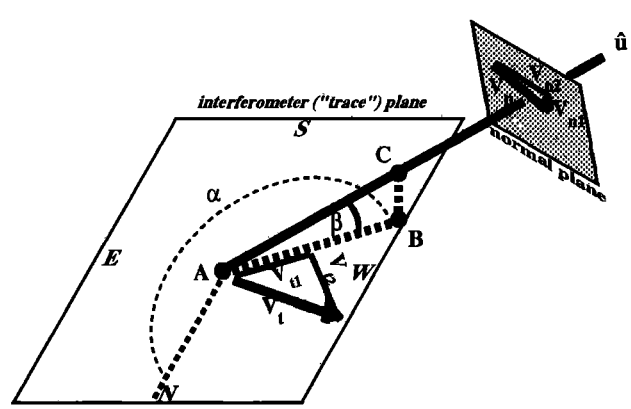

Figure A1. Relationship of interferometer plane and "normal" plane, which is normal to the line of sight $\hat{\mathbf{u}}$, and relationship of the trace velocity $\mathbf{V}_t$ in the interferometer plane and the projection $\mathbf{V}_n$ of this into the normal plane.

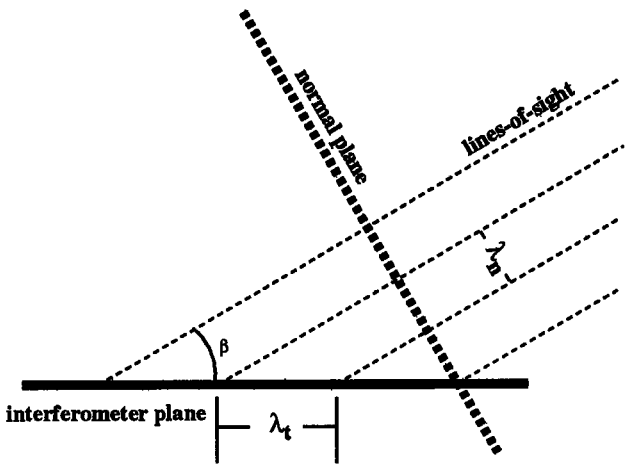

Figure A2. Relationship of trace and normal wavelengths, for the simple case of a linear array all of whose stations lie in the vertical plane containing the line of sight.

A2. Demagnification Factor

There is a second factor tending to make the trace spatial scales on the ground larger than physical spatial scales at the site of the irregularity. The lines of sight from the interferometer-array stations all converge together at the satellite (see Figure A3). Letting D_{is} be the distance from the irregularity to the satellite, and letting D_{gs} be the distance from the ground array to the satellite, then obviously the ground baseline b_g maps down to a demagnified in situ baseline b_i as follows:

$$\frac{b_i}{b_g} = \frac{D_{is}}{D_{gs}} \tag{A3}$$

In effect the interferometer is a microscope, whose power depends monotonically on the distance along the line of sight to the irregularity. However, unlike the first scale-magnification effect (see A1 above), this second effect is isotropic. Corrolary to the magnification effect just mentioned, the in situ normal velocity $\mathbf{V}_{nis}$ is parallel to $\mathbf{V}_n$ (see A2-A3 above) but slower:

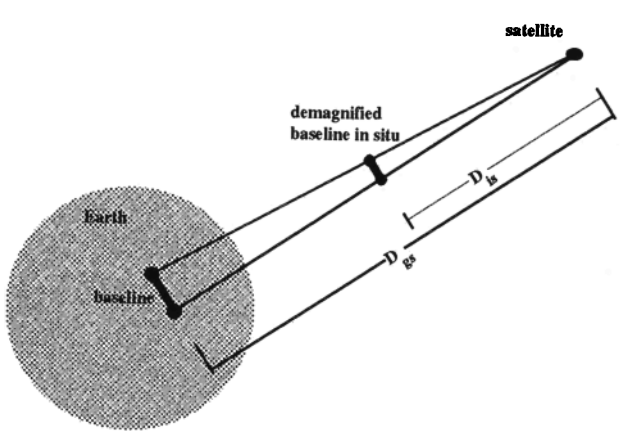

Figure A3. Illustration of the manner in which the ground level phase image is spatially magnified relative to the in situ electron density perturbation.

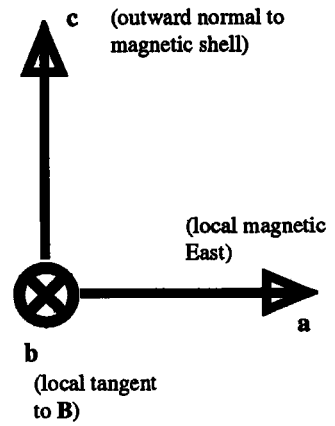

Figure A4. Illustration of the plane normal to the magnetic field **B** at the site of the irregularity.

$$\mathbf{V}_{nis} = \frac{D_{is}}{D_g}\mathbf{V}_n \tag{A4}$$

A3. Transformation Between Normal-Plane and Plane Perpendicular to B

Figure A4 shows the plane normal to the geomagnetic field **B** at the irregularity. Let **b** be the unit vector along **B**, let **a** be the unit vector magnetic eastward in the L shell, and let **c** be the outward normal to the L shell. Then the vector projections of **a** and **c** into the plane normal to the line of sight are

$$\mathbf{a}_n = \mathbf{a} - (\mathbf{u}\cdot\mathbf{a})\mathbf{u} \tag{A5}$$

$$\mathbf{c}_n = \mathbf{c} - (\mathbf{u}\cdot\mathbf{c})\mathbf{u} \tag{A6}$$

Physically, all **EXB** drifts are (by definition) normal to **B**, while the only motions which can be sensed by the interferometer are normal to **u** [*Jacobson and Erickson*, 1993]. Therefore the visibility of **EXB** drifts in the plasmasphere depends in a very complicated, though straightforwardly calculable, way on the geometry of the line-of-sight's path through the plasmasphere. The present data analysis assumes, on the basis of compelling evidence, that the sensed drifts in the normal plane are due to **EXB** drifts in the **a** (or -**a**) sense. Therefore we infer from a given in situ normal velocity $\mathbf{V}_{nis}$ an in situ magnetic east velocity according to the inverse of $|\mathbf{a}_n|$:

$$\frac{|\mathbf{V}|_{ais}}{|\mathbf{V}|_{nis}} = \frac{1}{|\mathbf{a} - (\mathbf{u}\cdot\mathbf{a})\mathbf{u}|} \tag{A7}$$

Notice that unlike the previous two transformations, this tends to reduce, not increase, the trace speed sensed by the interferometer.

A4. Transformation to Mapped *F* Layer on Same Field Line for Zonal Drift

In order to provide a zonal drift measure comparable to those of low-Earth-orbit satellites and ground-based incoherent scatter, we perform a mapping down the field line from the irregularity to the F layer (arbitrarily defined here as 300-km altitude). Neighboring magnetic meridian planes are separated by a constant angle. In terms of curvilinear arclength in the zonal sense, their separation varies as the cylindrical

radius from the dipole axis. Assuming that zonal drift is manifested as "rigid" zonal revolution of the field line about the magnetic dipole axis (equivalent to assuming that the field line is an isopotential), it follows that the zonal drift of a given field line varies as cylindrical radius also. The cylindrical radius r_c to the geomagnetic dipole axis is given by

$$r_c = r\cos\Lambda \tag{A8}$$

where r is the spherical radius and Λ is the magnetic latitude. The equation of a dipole field line is given by [*Mozer*, 1970]

$$r = L\cos^2\Lambda \tag{A9}$$

It follows that the F layer magnetic-east drift V_{af} is related to the in situ magnetic-east drift V_{ais} according to

$$\frac{V_{af}}{V_{ais}} = \left(\frac{r_f}{r_i}\right)^{3/2} \tag{A10}$$

where r_f and r_i are the spherical radii to the F layer and to the irregularity, respectively.

Acknowledgments. This work was performed under the auspices of the United States Department of Energy.

The Editor thanks J. A. Fennelly and another referee for their assistance in evaluating this paper.

References

Angerami, J. J., Whistler duct properties deduced from VLF observations with the Ogo 3 satellite near the geomagnetic equator, *J. Geophys. Res.*, *75*, 6115-6135, 1970.

Bertel, L., F. Bertin, and J. Testud, De la mesure du contenu électronique intégré appliquée à l'observation des ondes de gravité de moyenne échelle, *J. Atmos. Terr. Phys.*, *38*, 261-270, 1976.

Blanc, M, Magnetospheric convection effects at mid-latitudes, 1, Saint-Santin observations, *J. Geophys. Res.*, *88*, 211-223, 1983.

Buonsanto, M. J., and J. C. Foster, Effects of magnetospheric electric fields and neutral winds on the low-middle latitude ionosphere during the March 20-21, 1990 storm, *J. Geophys. Res.*, *98*, 19,133-19,140, 1992.

Buonsanto, M. J., M. E. Hagan, J. E. Salah, and B. G. Fejer, Solar cycle and seasonal variations in F-region electrodynamics at Millstone Hill, *J. Geophys. Res.*, *98*, 15,677-15,683, 1993.

Burgess, W. C., and U. S. Inan, The role of ducted whistlers in the precipitation loss and equilibrium flux of radiation belt electrons, *J. Geophys. Res.*, *98*, 15,643-15,665, 1993.

Carlos, R. C. , and R. S. Massey, The Los Alamos beacon receiver array, *IEEE Trans. Geosci. Remote Sens.*, *32*, 954-958, 1994.

Carpenter, D. L., Whistler studies of the plasmapause in the magnetosphere 1, *J. Geophys. Res.*, *71*, 693-709, 1966.

Carpenter, D. L., B. L. Giles, C. R. Chappell, P. M. E. Décréau, R. R. Anderson, A. M. Persoon, A. J. Smith, Y. Corcuff, and P. Canu, Plasmasphere dynamics in the duskside bulge region: A new look at an old topic, *J. Geophys. Res.*, *98*, 19,243-19,271, 1993.

Earle, G. D., and M. C. Kelley, Spectral studies of the sources of ionospheric electric fields, *J. Geophys. Res.*, *92*, 213-224, 1987.

Fejer, B. G., F-Region plasma drifts over Arecibo: Solar cycle, seasonal, and magnetic activity effects, *J. Geophys. Res.*, *98*, 13645-13652, 1993.

Fejer, B. G., and L. Scherliess, Time dependent response of equatorial ionospheric electric fields to magnetospheric disturbances, *Geophys. Res. Lett.*, *22*, 851-854, 1995.

Ganguly, S., R. A. Behnke, and B. A. Emery, Average electric field behavior in the ionosphere above Arecibo, *J. Geophys. Res.*, *92*, 1199-1210, 1987.

Georges, T. M., and W. H. Hooke, Wave-induced fluctuations in ionospheric electron content: A model indicating some observational biases, *J. Geophys. Res.*, *75*, 6295-6308, 1970.

Gonzales, C. A., et al., On the latitudinal variations of the ionospheric electric field during magnetospheric disturbances, *J. Geophys. Res.*, *88*, 9135-9144, 1983.

Hamar, D., G. Tarcsai, J. Lichtenberger, A. J. Smith, and K. H. Yearby, Fine structure of whistlers recorded digitally at Halley, Antarctica, *J. Atmos. Terr. Phys.*, *52* , 801-810, 1990.

Hanson, W. B., and F. S. Johnson, Lower midlatitude ionospheric disturbances and the Perkins instability, *Planet. Space Sci.*, *40*, 1615-1630, 1992.

Heelis, R. A., and W. R. Coley, East-West ion drifts at mid-latitudes observed by Dynamics Explorer 2, *J. Geophys. Res.*, *97*, 19,461-19,469, 1992.

Horwitz, J. L., R. H. Comfort, and C. R. Chappel, A statistical characterization of plasmasphere density structure and boundary locations, *J. Geophys. Res.*, *95*, 7937-7947, 1990.

Huang, C.-S., and M. C. Kelley, Nonlinear evolution of equatorial spread-F: 1, On the role of plasma instabilities and spatial resonance associated with gravity wave seeding, *J. Geophys. Res.*, *101*, 283-292, 1996.

Huang, T. S., R. A. Wolf, and T. W. Hill, Interchange instability of the Earth's plasmapause, *J. Geophys. Res.*, *95*, 17,187-17,198, 1990.

Jacobson, A. R., and W. C. Erickson, A method for characterizing transient ionospheric disturbances using a large radiotelescope array, *Astron. Astrophys.*, *257*, 401-409, 1992a.

Jacobson, A. R., and W. C. Erickson, Wavenumber-resolved observations of ionospheric waves using the Very Large Array radiotelescope, *Planet. Space Sci.*, *404*, 447-455, 1992b.

Jacobson, A. R., and W. C. Erickson, Observations of electron density irregularities in the plasmasphere using the VLA radio-interferometer, *Ann. Geophys.*, *11*, 869-888, 1993.

Jacobson, A. R., R. C. Carlos, R. S. Massey, and G. Wu, Observations of traveling ionospheric disturbances with a satellite-beacon radio-interferometer: Seasonal and local-time behavior, *J. Geophys. Res.*, *100*, 1653-1665, 1995a.

Jacobson, A. R., R. C. Carlos, R. S. Massey, G. Wu, and G. Hoogeveen, Total-electron-content signatures of plasmaspheric motions, *Geophys. Res. Lett.*, *22*, 2461-2464, 1995b.

Kelley, M. C., C. L. Siefring, R. F. Pfaff, P. M. Kintner, M. Larsen, R. Green, R.H. Holzworth, L.C. Hale, J.D. Mitchell, and D. Le Vine, Electrical measurements in the atmosphere and the ionosphere over an active thunderstorm, 1, Campaign overview and initial ionospheric results, *J. Geophys. Res.*, *90*, 9815-9823, 1985.

Kelley, M. C., Intense sheared flow as the origin of large-scale undulations of the edge of the diffuse aurora, *J. Geophys. Res.*, *91*, 3225-3230, 1986.

Kelley, M. C., J. G. Ding, and R. H. Holzworth, Intense ionospheric electric and magnetic field pulses generated by lightning, *Geophys. Res. Lett.*, *17*, 2221-2224, 1990.

Kintner, P. M., and C. E. Seyler, The status of observations and theory of high latitude ionospheric and magnetospheric plasma turbulence, *Space Sci. Rev*, *41*, 91-129, 1985.

Kraichnan, R.H., Inertial ranges in two-dimensional turbulence, *Phys. Fluids 10*, 1417-1423, 1967.

LeDocq, M. J., D. A. Gurnett, and R. R. Anderson, Electron number density fluctuations near the plasmapause observed by the CRRES spacecraft, *J. Geophys. Res.*, *99*, 23,661-23,671, 1994.

Lui, A. T., Y., C. - I. Meng, and S. Ismail, Large amplitude undulations on the equatorward boundary of the diffuse aurora, *J. Geophys. Res.* *87*, 2385-2400, 1982.

Mendillo, M., J. B. Baumgardner, and J. Providakes, Ground-based imaging of detached arcs, ripples in the diffuse aurora, and patches of 6300-Å CV emission, *J. Geophys. Res.*, *94*, 5367 - 5381, 1989.

Mercier, C., Observations of atmospheric gravity waves by radiointerferometry, *J. Atmos. Terr. Phys.*, *4*, 605-624, 1986.

Miller, C.A., On gravity waves and the electrodynamics of the mid-latitude ionosphere, Ph.D. thesis, Cornell Univ., Ithaca, N.Y., 1996.

Mozer, F. S., Electric field mapping in the ionosphere at the equatorial plane, *Planet. Space Sci.*, *18*, 259-263, 1970.

Oliver, W. L., Y. Yamamoto, T. Takami, S. Fukao, and T. Tsuda, Middle and upper atmosphere radar observations of ionospheric electric fields, *J. Geophys. Res.*, *98*, 11,615-11,627, 1993.

Park, C. G., and R. A. Helliwell. The formation of field-aligned irregularities in the magnetosphere, *Radio Sci.*, *6*, 299 - 304, 1971.

Richmond, A. D., Self-induced motions of thermal plasma in the magnetosphere and the stability of the plasmapause, *Radio Sci.*, *8*, 1019-1027, 1973.

Smiddy, M., M .C. Kelley, W. Burke, R. Rich, R. Sagalyn, B. Shuman, R. Hays, and S. Lai, Intense poleward-directed electric fields near the ionospheric projection of the plasmapause, *Geophys. Res. Lett.*, *4*, 543 - 546, 1977.

Sonwalker, V. S., U. S. Inan, T. F. Bell, R. A. Helliwell, V. M. Chmyrev, Ya. P. Sobolev, O. Ya. Ovcharenko, and V. Selegej, Simultaneous observations of VLF ground transmitter signals on the DE 1 and COSMOS 1809 satellites: Detection of a magnetospheric caustic and a duct, *J. Geophys. Res.*, *99*, 17,511-17,522, 1994.

Spiro, R.W., R.A. Heelis, and W.B. Hanson, Rapid subauroral ion drifts observed by Atmospheric Explorer C, *Geophys. Res. Lett.*, *6*, 657-660, 1978.

Tsyganenko, N. A., A magnetospheric magnetic field model with a warped tail current sheet, *Planet. Space Sci.*, *37*, 5-20, 1989.

Vinas, A. F., and T. R. Madden, Shear flow-ballooning instability as a possible mechanism for hydromagnetic fluctuations at the plasmapause, *J. Geophys. Res.*, *91*, 1519 - 1528, 1986.

Wand, R. H., A model representation of the ionospheric electric field over Millstone Hill ($\Lambda = 56°$), *J. Geophys. Res.*, *86*, 5801-5808, 1981.

Wand, R. H., and J. V. Evans, The penetration of convection electric fields to the latitude of Millstone Hill ($\Lambda = 56°$), *J. Geophys. Res. 86*, 5809-5814, 1981.

Yamamoto, T., K. Makita, and C. - I. Meng, A particle simulation of large-amplitude undulations on the evening diffuse auroral boundary, *J. Geophys. Res.*, *96*, 1439-1449, 1991.

Yamamoto, T., M. Ozaki, S. Inoue, K. Makita, and C. - I. Meng. Convective generation of "giant"0 undulations on the evening diffuse auroral boundary, *J. Geophys. Res.*, *99*, 19,499-19,512, 1994.

Yeh, H.-C., J. C. Foster, F. J. Rich, and W. Swider, Storm time electric field penetration observed at mid-latitude, *J. Geophys. Res.*, *96*, 5707-5721, 1991.

R. C. Carlos, G. Hoogeveen, A. R. Jacobson and G. Wu, Space and Atmospheric Sciences Group, Los Alamos National Laboratory, Los Alamos, NM 87545

B. G. Fejer, Center for Atmospheric and Space Sciences, Utah State Unversity, Logan, UT 84322

M. C. Kelley, School of Electrical Engineering, Cornell University, Ithaca, NY 14853

(Received November 7, 1995; revised April 16, 1996; accepted April 17, 1996.)